Title: Glioblastomas derived from genetically modified pluripotent stem cells recapitulate pathobiology

Authors: Tomoyuki Koga[1], Jorge A. Benitez[1]*, Isaac A. Chaim[2]*, Sebastian Markmiller[2]*, Alison D. Parisian[1,3], Kristen M. Turner[1], Florian M. Hessenauer[1], Matteo D'Antonio[4], Nam-phuong D. Nguyen[5], Shahram Saberi[6], Jianhui Ma[1], Shunichiro Miki[1], Antonia D. Boyer[1], John Ravits[6], Kelly A. Frazer[4,7], Vineet Bafna[5], Clark C. Chen[8], Paul S. Mischel[1,3], Gene W. Yeo[2]†‡, and Frank B. Furnari[1,3]†‡.

Affiliations:

[1]Ludwig Cancer Research, San Diego Branch, La Jolla, CA 92093, USA.

[2]Department of Cellular and Molecular Medicine, University of California at San Diego, La Jolla, CA 92093, USA.

[3]Department of Pathology, University of California at San Diego, La Jolla, CA 92093, USA.

[4]Institute for Genomic Medicine, University of California at San Diego, La Jolla, CA 92093, USA.

[5]Department of Computer Science and Engineering, University of California at San Diego, La Jolla, CA 92093, USA.

[6]Department of Neuroscience, University of California at San Diego, La Jolla, CA 92093, USA.

[7]Department of Pediatrics and Rady Children's Hospital, University of California at San Diego, La Jolla, CA 92093, USA.

[8]Department of Neurosurgery, University of Minnesota, Minneapolis, MN 55455, USA.

*These authors contributed equally to this work.

†This work is based on equal contributions from the laboratories of G.W.Y, and F.B.F.

‡Correspondence to: Frank B. Furnari, Ludwig Cancer Research, University of California at San Diego, 9500 Gilman Dr., CMM-East Room 3055, La Jolla, CA, 92093-0660. Phone: 858-534-7819. Fax: 858-534-7750. Email: ffurnari@ucsd.edu

‡Gene W. Yeo, Dept of Cellular and Molecular Medicine, University of California at San Diego, 2880 Torrey Pines Scenic Drive, La Jolla, CA 92037. Phone: 858 534 9321. Email: geneyeo@ucsd.edu

Abstract: Glioblastoma (GBM) is the most common malignant brain tumor, and particularly difficult to treat due to its inherent heterogeneity, which is promoted by a variety of genetic drivers. A lack of models that robustly recapitulate heterogeneity has been a major obstacle for research progress on this disease. Here we show that neural progenitor cells derived from human induced pluripotent stem cells, CRISPR/Cas9 engineered with different combinations of authentic GBM-related genetic drivers give rise to GBM models that recapitulate the pathobiology of this tumor, including inter- and intra-tumor heterogeneity, differential drug sensitivity, extrachromosomal DNA amplifications, and rapid clonal evolution. Different models

established with this approach could serve as a platform for longitudinal assessment of drug treatment sensitivity governed by subtype-specific driver mutations.

One Sentence Summary: hiPSC-derived GBMs recapitulate disease.

Main Text: GBM, the most common primary malignant tumor of the central nervous system (*1*), has been studied using different varieties of tumor models. Transgenic mouse models (*2*) and engineered human astrocyte-derived models (*3, 4*) have been utilized for decades, but application of exogenous viral factors such as SV40 T/t-Ag, HPV E6, and E7, or mutations of genes not commonly affected in GBM such as Src, K-ras, and H-ras have the potential to make these models dissimilar to the actual disease. Patient derived xenograft (PDX) models do overcome such limitations (*5*), but acquired passenger mutations make it difficult to study the effect of each driver mutation on different characteristics of this disease, and their direct effects on tumor initiation and evolution can only be inferred based on single cell sequencing and phylogenetic relationships.

We reasoned that introducing combinations of mutations identified by The Cancer Genome Atlas (*6, 7*) as GBM driver mutations into human neural progenitor cells (NPCs), potential cells of origin of GBM (*8*), could generate a model for studying different types of GBM in the context of an isogenic background. We first introduced two different combinations of driver mutations into human induced pluripotent stem cells (iPSCs) by CRISPR/Cas9 genome editing (*9, 10*) (Fig. 1, A and B). One combination of deletions targeted tumor suppressor genes *PTEN* and *NF1*, which are commonly altered together in mesenchymal subtype of GBM (*6, 7*). A second combination of deletions targeted *TP53* and exon 8 and 9 of *PDGFRA* (*PDGFRAΔ8-9*). This creates a constitutively active truncating PDGFRA mutation observed in 40% of *PDGFRA* amplified GBM (*11*), resulting in a genotype common in the proneural subtype of isocitrate dehydrogenase-wildtype GBM (*6, 7*). The genetic modifications in single clones were confirmed by genotyping PCR (fig. S1) and RT-PCR (Fig. 1C). Edited iPSC clones with desired mutations were differentiated into NPCs, using a small molecule protocol (*12*) and differentiation status was confirmed by downregulation of pluripotency markers, Nanog and Oct4, and corresponding upregulation of NPC markers, Pax6, Nestin, and Sox1 (fig. S2). Confirmation of a neural progenitor state was illustrated by further differentiation into astrocytes, neurons, and oligodendrocytes (fig. S3).

We next evaluated if these genetically modified NPCs were capable of forming orthotopic tumors in immunocompromised mice (Fig. 1A). When edited NPCs were engrafted in the brains of Nod/Scid mice, $PTEN^{-/-};NF1^{-/-}$ NPCs and $TP53^{-/-};PDGFRA^{wt/\Delta 8\text{-}9}$ NPCs both formed brain tumors (Fig. 1D) with a latency of six to nine months. Pathological assessment of these tumors revealed regions of hypercellularity, positivity for GFAP and Olig2, and high expression of Ki-67, features consistent with aggressive tumors with GBM phenotype (Fig. 1D). In contrast, $PTEN^{-/-}$ and $TP53^{-/-}$ singly edited NPCs did not form tumors in the brain over the same time span (fig. S4, A and B), while unedited iPSCs formed teratoma-like tumors (fig. S5). Lack of teratomas after NPC injection suggests a high efficiency of differentiation to NPCs with the small molecule protocol. These results illustrate that small numbers of known driver mutations found in GBM are sufficient for phenotypic recapitulation of human tumors in this model system.

One of the benefits of using PDX models in cancer research is that they can be cultured *in vitro* and be re-engrafted in animals, thus enabling both *in vitro* and *in vivo* analyses (*13*). We

evaluated if our induced GBM (iGBM) models could be used in a similar manner. Dissociated tumors obtained from the mouse brains were FACS sorted for human cells using a human MHC antibody, followed by propagation of isolated cells in the same neurosphere conditions used for GBM PDX spheres (*14*), which confirmed iGBM sphere formation capability (Fig. 2A). These iGBM spheres possessed the same genotypes as the corresponding input NPCs (fig. S6). Extreme limiting dilution assays (*15*) showed that iGBM spheres had greater self-renewal capacity, a feature of cancer stem cells, when compared to pre-engraftment NPCs (Fig. 2B), again highlighting gain of cancerous phenotypes of iGBM cells compared to original input cells. The finding that only subpopulations of iGBM sphere cells expressed CD133, (Fig. 2C) a neural stem cell marker (*16*), while input NPCs were homogeneously positive for CD133 (fig. S7), further suggests intra-tumor heterogeneity in iGBM subpopulations displaying a cancer stem cell phenotype (*17*). We then evaluated if these iGBM-derived sphere cells maintained tumorigenic capacity by secondary orthotopic engraftment (Fig. 2D). When injected in the brains of Nod/Scid mice, iGBM-derived sphere cells formed tumors with a shortened latency period of one to two months (Fig. 2E). The cells obtained from these secondary iGBM tumors had even greater self-renewal capabilities compared with sphere cells obtained from the primary tumors (fig. S8), suggesting further malignant transformation through *in vivo* passage. We also tested if these models can be used for *in vivo* drug treatment experiments comparable to those applied to PDX lines by treating orthotopically engrafted animals with temozolomide (TMZ), a DNA-alkylating chemotherapeutic agent used for standard care treatment of GBM patients (*18*). *TP53*$^{-/-}$*;PDGFRA*$^{wt/\Delta 8\text{-}9}$ iGBMs proved to be more sensitive to TMZ compared to *PTEN*$^{-/-}$*;NF1*$^{-/-}$ iGBMs (Fig. 2F). *PTEN*$^{-/-}$*;NF1*$^{-/-}$ iGBMs were found to express higher levels of O^6-methylguanine DNA methyl transferase (MGMT) (Fig. 2G), which is associated with resistance to TMZ in GBM patients (*19*), compared to *TP53*$^{-/-}$*;PDGFRA*$^{wt/\Delta 8\text{-}9}$ iGBMs, a possible explanation of this differential sensitivity, although MGMT-independent mechanisms in the context of *TP53* alteration (*20, 21*) cannot be eliminated.

We previously reported that extrachromosomal DNA (ecDNA) is prevalent in many cancer types, especially in GBM, and that ecDNA is associated with resistance to drug treatment and rapid evolution of tumor heterogeneity (*22, 23*). To determine if our iGBM models recapitulated the generation of ecDNA, we first investigated if the original input NPCs possessed karyotype abnormalities or traces of ecDNA. Based on DAPI staining of metaphase spreads and digital karyotyping, edited NPC were karyotypically normal (fig. S9 and S10) as were *PTEN*$^{-/-}$*;NF1*$^{-/-}$ iGBM cells (Fig. 3A). In sharp contrast, metaphase spreads of cells obtained from *TP53*$^{-/-}$*;PDGFRA*$^{wt/\Delta 8\text{-}9}$ iGBMs showed small DAPI-stained dots adjacent to chromosomes, suggestive of ecDNA (Fig. 3B), consistent with our previous findings in GBM tumor samples (*23*). Furthermore, double minute-like structures became more apparent in the secondary tumors obtained by re-engraftment of the primary spheres (Fig. 3C). Those ecDNA incorporated EdU, suggesting replication of those extrachromosomal components (Fig. 3D). The *TP53*$^{-/-}$*;PDGFRA*$^{wt/\Delta 8\text{-}9}$ iGBMs also presented striking numerical and structural chromosome alterations (Fig. 3E). This is the first human stem cell-derived cancer model presenting with spontaneous extrachromosomal DNA amplifications, a frequently observed genomic characteristic of cancer (*23*). The involvement of TP53 in this model might have been crucial for the formation of ecDNA as has been seen in previous mouse model studies (*24, 25*).

We further investigated if these iGBMs showed inter- and intra-tumor heterogeneities, which are other notable hallmarks of GBM (*26*), and have not been recapitulated by previous models. First, the pattern of invasiveness was strikingly different between the two models, with *PTEN*$^{-/-}$

;NF1$^{-/-}$ iGBM showing more prominent diffuse invasion compared with *TP53*$^{-/-}$*;PDGFRA*$^{wt/\Delta 8\text{-}9}$ iGBM (fig. S11). These tumors were different as well in terms of transcriptomes. Single-cell RNA sequencing (scRNA-seq) was performed using primary iGBM spheres, secondary iGBM tumor cells obtained from orthotopic injection of the primary spheres, and secondary spheres obtained by *in vitro* culture of the secondary tumor cells (Fig. 4A). Transcriptome profiles varied between primary and secondary spheres of the same genotype as well as between spheres and tumors, but the greatest variation occurred between the two iGBM models of different genotypes (Fig. 4, B and C, fig. S12). This is suggestive of inter-tumor heterogeneity between iGBM models which wasnot apparent in pre-engraftment NPCs with different gene edits (fig. S13). These findings suggest that a small number of key driver mutations play an important role in developing such pathognomonic inter-tumor heterogeneity that arises through the process of transformation. When GBM subtype specific genes were analyzed, *TP53*$^{-/-}$*;PDGFRA*$^{wt/\Delta 8\text{-}9}$ iGBM showed upregulation of genes characteristic of the proneural subtype, while the *PTEN*$^{-/-}$*;NF1*$^{-/-}$ iGBM showed a mesenchymal subtype signature (Fig. 4D, fig. S14, tables S1 to S4). However, when examined at single cell resolution, each sample shows intra-tumor heterogeneity with different populations of cells presenting signatures of different subtypes (Fig. 4E, fig. S14), as is observed in actual GBM patient samples (*26*). Within each iGBM model, there existed populations of cells with variations in cell cycle (Fig. 4F, fig. S15) and stemness signatures (Fig. 4G, fig. S16), resembling populations present in patient GBM tumors (*26*). Furthermore, *TP53*$^{-/-}$*;PDGFRA*$^{wt/\Delta 8\text{-}9}$ iGBM presented greater diversity compared to the *PTEN*$^{-/-}$*;NF1*$^{-/-}$ model (Fig. 4C, fig. S17), both between samples from different tumor passages (primary vs secondary tumors and spheres) or replicates from different animals. This suggests a clonally unstable nature of the *TP53*$^{-/-}$*;PDGFRA*$^{wt/\Delta 8\text{-}9}$ model, where genomic instability or ecDNA could be driving dynamic clonal evolution (*23, 27*).

In summary, we generated a robust system to model human glioblastoma. By introducing different combinations of essential genetic alterations into human iPSCs, resulting tumors faithfully recapitulated hallmarks of GBM pathobiology including histology, gene expression signatures, inter- and intra-tumor heterogeneity, and clonal evolution. Each model presents different characteristics depending on the background genetic alterations, and thus, we expect this to be a useful platform for examining phenotypes resulting from genetic alterations of GBM and other cancer types to derive effective treatments based on specific driver mutations.

References and Notes:

1. T. F. Cloughesy, W. K. Cavenee, P. S. Mischel, Glioblastoma: from molecular pathology to targeted treatment. *Annu Rev Pathol* **9**, 1-25 (2014).
2. S. S. Stylli, R. B. Luwor, T. M. Ware, F. Tan, A. H. Kaye, Mouse models of glioma. *J Clin Neurosci* **22**, 619-626 (2015).
3. J. N. Rich *et al.*, A genetically tractable model of human glioma formation. *Cancer Res* **61**, 3556-3560 (2001).
4. Y. Sonoda *et al.*, Formation of intracranial tumors by genetically modified human astrocytes defines four pathways critical in the development of human anaplastic astrocytoma. *Cancer Res* **61**, 4956-4960 (2001).
5. Y. Xie *et al.*, The Human Glioblastoma Cell Culture Resource: Validated Cell Models Representing All Molecular Subtypes. *EBioMedicine* **2**, 1351-1363 (2015).

6. R. G. Verhaak *et al.*, Integrated genomic analysis identifies clinically relevant subtypes of glioblastoma characterized by abnormalities in PDGFRA, IDH1, EGFR, and NF1. *Cancer Cell* **17**, 98-110 (2010).
7. C. W. Brennan *et al.*, The somatic genomic landscape of glioblastoma. *Cell* **155**, 462-477 (2013).
8. J. H. Lee *et al.*, Human glioblastoma arises from subventricular zone cells with low-level driver mutations. *Nature* **560**, 243-247 (2018).
9. L. Cong *et al.*, Multiplex genome engineering using CRISPR/Cas systems. *Science* **339**, 819-823 (2013).
10. M. Jinek *et al.*, RNA-programmed genome editing in human cells. *Elife* **2**, e00471 (2013).
11. T. Ozawa *et al.*, PDGFRA gene rearrangements are frequent genetic events in PDGFRA-amplified glioblastomas. *Genes Dev* **24**, 2205-2218 (2010).
12. P. Reinhardt *et al.*, Derivation and expansion using only small molecules of human neural progenitors for neurodegenerative disease modeling. *PLoS One* **8**, e59252 (2013).
13. C. Pauli *et al.*, Personalized In Vitro and In Vivo Cancer Models to Guide Precision Medicine. *Cancer Discov* **7**, 462-477 (2017).
14. D. Akhavan *et al.*, De-repression of PDGFRbeta transcription promotes acquired resistance to EGFR tyrosine kinase inhibitors in glioblastoma patients. *Cancer Discov* **3**, 534-547 (2013).
15. Y. Hu, G. K. Smyth, ELDA: extreme limiting dilution analysis for comparing depleted and enriched populations in stem cell and other assays. *J Immunol Methods* **347**, 70-78 (2009).
16. N. Uchida *et al.*, Direct isolation of human central nervous system stem cells. *Proc Natl Acad Sci U S A* **97**, 14720-14725 (2000).
17. S. K. Singh *et al.*, Identification of a cancer stem cell in human brain tumors. *Cancer Res* **63**, 5821-5828 (2003).
18. R. Stupp *et al.*, Radiotherapy plus concomitant and adjuvant temozolomide for glioblastoma. *N Engl J Med* **352**, 987-996 (2005).
19. M. E. Hegi *et al.*, MGMT gene silencing and benefit from temozolomide in glioblastoma. *N Engl J Med* **352**, 997-1003 (2005).
20. M. D. Blough, D. C. Beauchamp, M. R. Westgate, J. J. Kelly, J. G. Cairncross, Effect of aberrant p53 function on temozolomide sensitivity of glioma cell lines and brain tumor initiating cells from glioblastoma. *J Neurooncol* **102**, 1-7 (2011).
21. Z. D. Nagel *et al.*, DNA Repair Capacity in Multiple Pathways Predicts Chemoresistance in Glioblastoma Multiforme. *Cancer Res* **77**, 198-206 (2017).
22. D. A. Nathanson *et al.*, Targeted therapy resistance mediated by dynamic regulation of extrachromosomal mutant EGFR DNA. *Science* **343**, 72-76 (2014).
23. K. M. Turner *et al.*, Extrachromosomal oncogene amplification drives tumour evolution and genetic heterogeneity. *Nature* **543**, 122-125 (2017).
24. C. V. Camacho *et al.*, DNA double-strand breaks cooperate with loss of Ink4 and Arf tumor suppressors to generate glioblastomas with frequent Met amplification. *Oncogene* **34**, 1064-1072 (2015).
25. H. Zou *et al.*, Double minute amplification of mutant PDGF receptor alpha in a mouse glioma model. *Sci Rep* **5**, 8468 (2015).

26. A. P. Patel *et al.*, Single-cell RNA-seq highlights intratumoral heterogeneity in primary glioblastoma. *Science* **344**, 1396-1401 (2014).
27. A. C. deCarvalho *et al.*, Discordant inheritance of chromosomal and extrachromosomal DNA elements contributes to dynamic disease evolution in glioblastoma. *Nat Genet* **50**, 708-717 (2018).
28. A. Gore *et al.*, Somatic coding mutations in human induced pluripotent stem cells. *Nature* **471**, 63-67 (2011).
29. F. A. Ran *et al.*, Genome engineering using the CRISPR-Cas9 system. *Nat Protoc* **8**, 2281-2308 (2013).
30. F. A. Wolf, P. Angerer, F. J. Theis, SCANPY: large-scale single-cell gene expression data analysis. Genome Biol 19, 15 (2018).
31. A. Dobin *et al.*, STAR: ultrafast universal RNA-seq aligner. *Bioinformatics* **29**, 15-21 (2013).
32. J. Harrow *et al.*, GENCODE: the reference human genome annotation for The ENCODE Project. *Genome Res* **22**, 1760-1774 (2012).
33. S. Anders, P. T. Pyl, W. Huber, HTSeq--a Python framework to work with high-throughput sequencing data. *Bioinformatics* **31**, 166-169 (2015).
34. S. Anders, A. Reyes, W. Huber, Detecting differential usage of exons from RNA-seq data. *Genome Res* **22**, 2008-2017 (2012).
35. M. I. Love, W. Huber, S. Anders, Moderated estimation of fold change and dispersion for RNA-seq data with DESeq2. *Genome Biol* **15**, 550 (2014).
36. S. Anders, W. Huber, Differential expression analysis for sequence count data. *Genome Biol* **11**, R106 (2010).

Acknowledgments: We thank W.K. Cavenee, A.H. Thorne, C. Zanca, and Furnari lab members for discussions and helpful suggestions. We are grateful to the IGM Genomics Center, University of California San Diego for conducting RNA sequencing, digital karyotyping, single-cell RNA sequencing and whole genome sequencing. We thank the Center for Advanced Laboratory Medicine, University of California San Diego for assistance with immunohistochemistry. We thank M. F. Camargo for providing graphical work. **Funding:** This work was supported by National Institutes of Health R01NS080939 (F.B.F.), the Defeat GBM Research Collaborative, a subsidiary of the National Brain Tumor Society (F.B.F., and P.S.M.), Ruth L. Kirschstein Institutional National Research Award T32 GM008666 (A.D.P.), grants from National Institute of Neurological Disorders and Stroke NS73831 (P.S.M.), the Ben and Catherine Ivy Foundation (P.S.M.), and National Institutes of Health P30CA023100 (IGM Genomics Center). **Author contributions:** T.K., Se.M., G.W.Y., and F.B.F conceived and designed the study. T.K., J.A.B., A.D.P., K.M.T., F.M.H., S.S., J.M., Sh.M., and A.D.B. conducted the experiments. I.A.C, N.D.N., and M.D.A. performed bioinformatics analyses. J.R., K.A.F., V.B., C.C.C., and P.S.M. supervised parts of the study. G.W.Y and F.B.F supervised all aspects of the study. T.K. and F.B.F. wrote the manuscript with inputs from other authors. **Competing interests:** P.S.M. is co-founder of Pretzel Therapeutics, Inc. He has equity and serves as a consultant for the company. PSM also did a one-time consultation for Abide Therapeutics, Inc. **Data and materials availability:** All data are available from the main text and supplementary materials.

Supplementary Materials:

Materials and Methods

Figures S1-S17

Tables S1-S4

References (28-36)

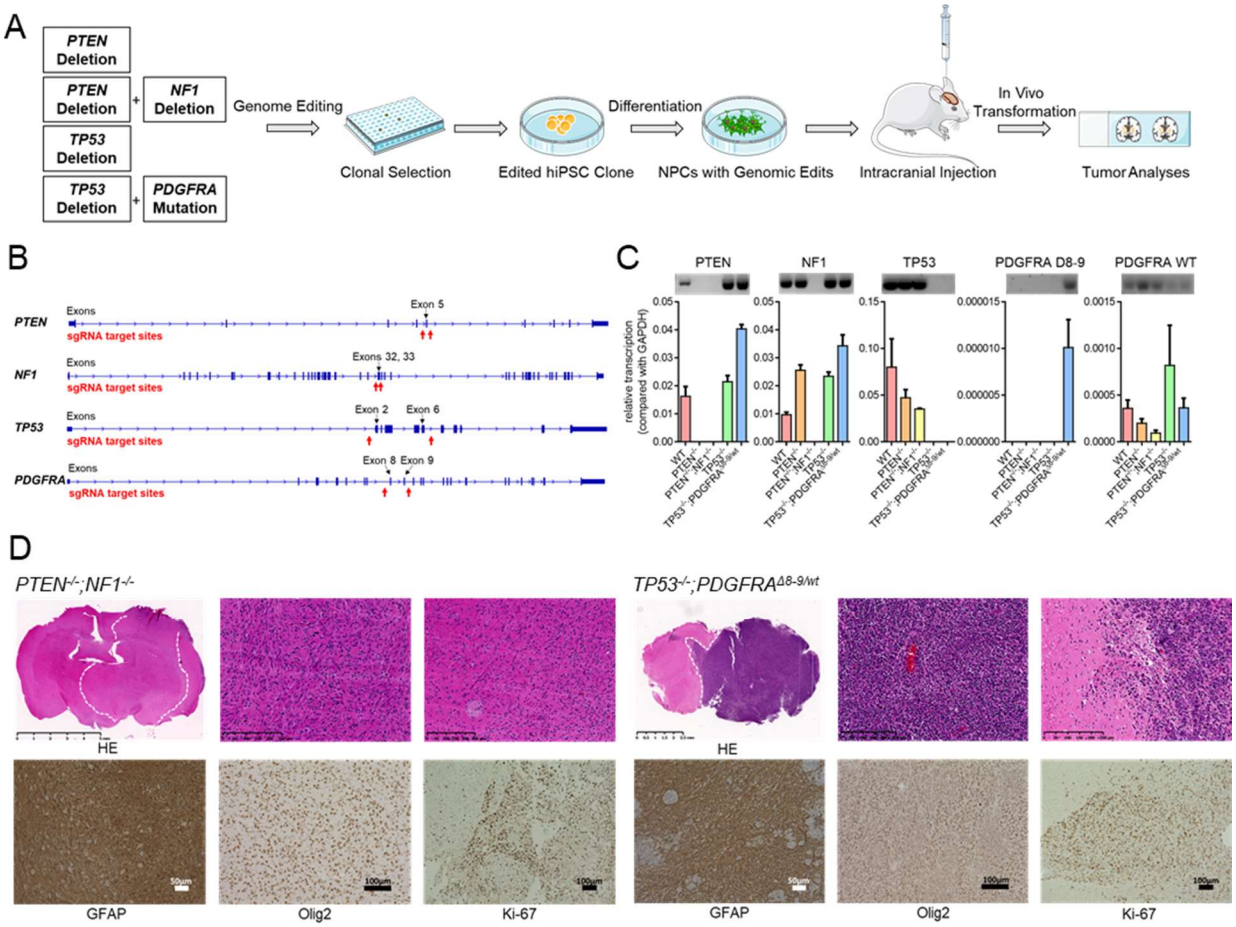

Fig. 1. Different iGBM models derived from edited human iPSCs. (A) Schema of iGBM generation. (B) Designs for gene editing indicating placement of sgRNAs. (C) RT-qPCR evaluating designated edits. (D) H&E, GFAP, Olig2, and Ki-67 staining of tumors generated from engrafted *PTEN*$^{-/-}$;*NF1*$^{-/-}$ NPCs and *TP53*$^{-/-}$;*PDGFRA*$^{wt/\Delta 8\text{-}9}$ NPCs.

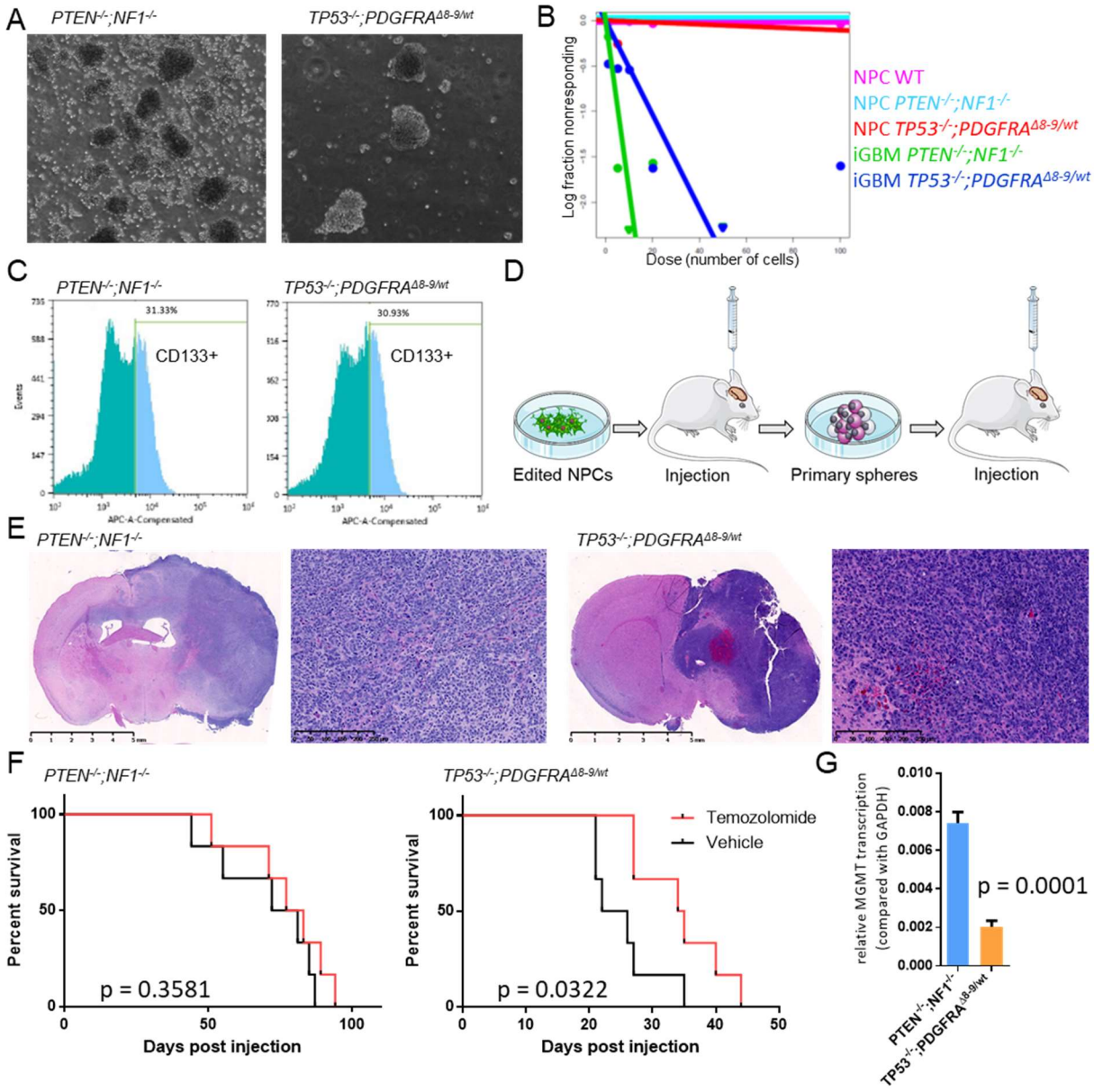

Fig. 2. iGBMs have cancer stem cell phenotype and can be used for *in vivo* drug testing. (A) iGBM spheres obtained by maintaining iGBM tumor cells in neurosphere culture conditions. (B) Extreme limiting dilution analysis of input NPCs and tumor-derived iGBM sphere cells. (C) CD133 staining of iGBM cells analyzed by flow cytometry. (D) Scheme of secondary iGBM xenograft tumor formation. (E) H&E staining of secondary xenograft tumors. (F) *In vivo* survival assays of mice orthotopically engrafted with primary iGBM sphere cells upon treatment either with vehicle or temozolomide. (G) MGMT expression levels in iGBM cells quantified by RT-qPCR.

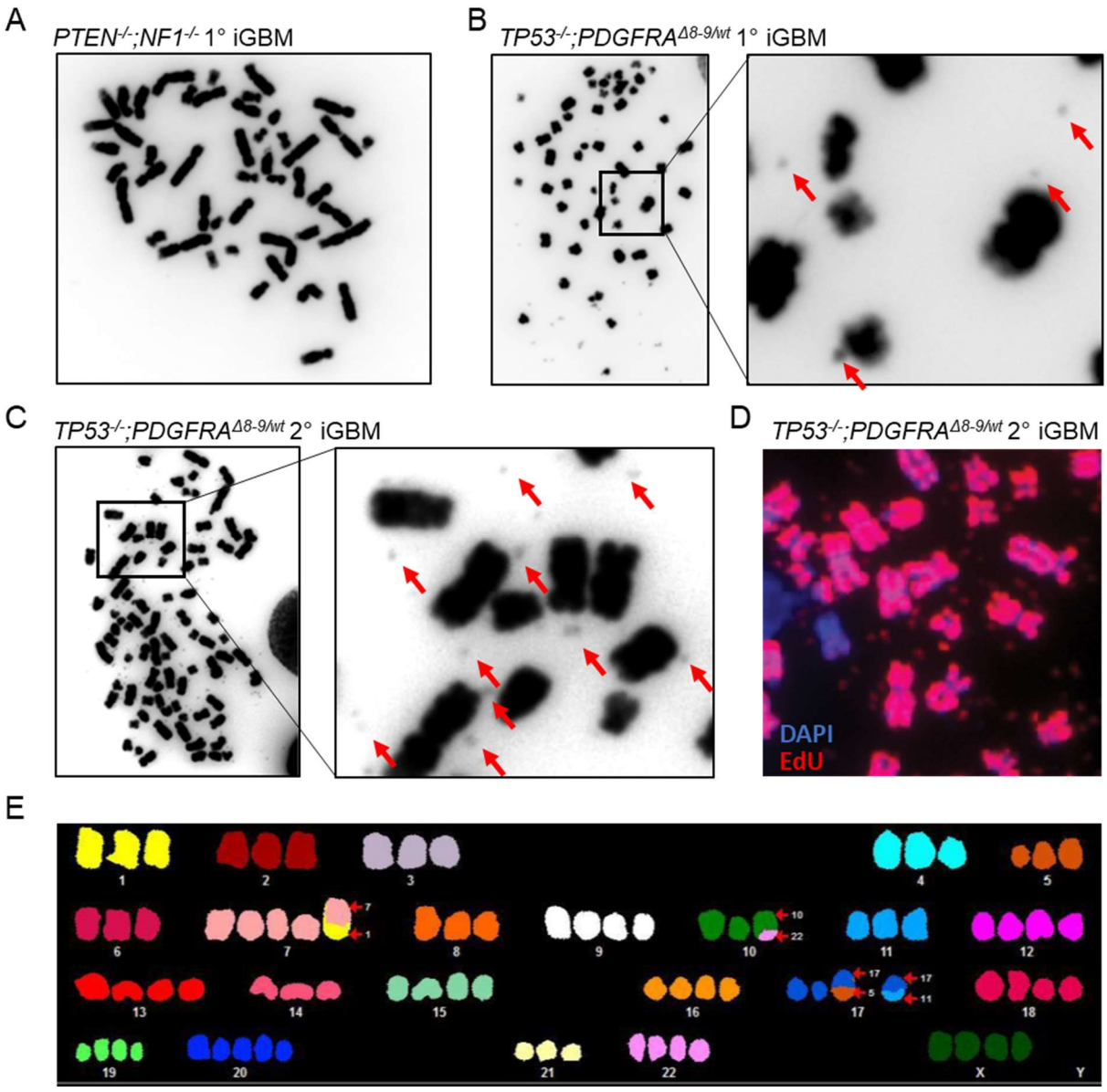

Fig. 3. *TP53*$^{-/-}$*;PDGFRA*$^{\Delta 8\text{-}9/wt}$ iGBM shows prominent karyotype abnormalities accompanied by extrachromosomal DNA. (A) DAPI staining of *PTEN*$^{-/-}$*;NF1*$^{-/-}$ primary iGBM cells. (B) DAPI staining of *TP53*$^{-/-}$*;PDGFRA*$^{wt/\Delta 8\text{-}9}$ primary iGBM cells. Red arrows indicate ecDNA. (C) DAPI staining of *TP53*$^{-/-}$*;PDGFRA*$^{wt/\Delta 8\text{-}9}$ secondary iGBM cells. Red arrows indicate ecDNA. (D) EdU labeling of chromosomes and ecDNA in a metaphase spread of *TP53*$^{-/-}$*;PDGFRA*$^{wt/\Delta 8\text{-}9}$ secondary iGBM. (E) Spectral karyotyping analysis of *TP53*$^{-/-}$*;PDGFRA*$^{wt/\Delta 8\text{-}9}$ iGBM cells.

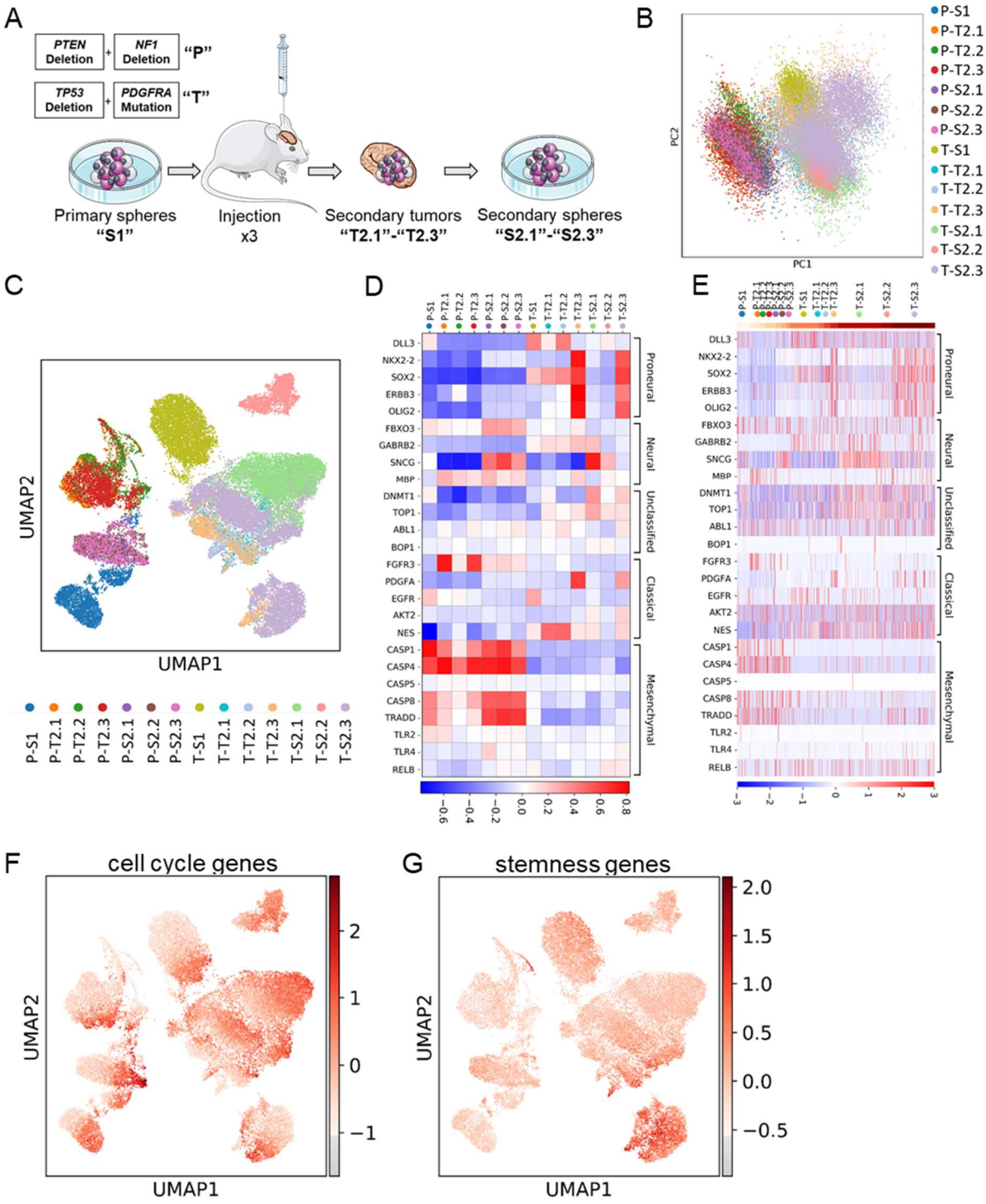

Fig. 4. iGBM models present inter- and intra-tumor heterogeneities and divergent transcriptomes. (A) Scheme of single-cell RNA sequencing experiments. Primary spheres (S1), secondary tumors (T2.1-T2.3), and secondary spheres (S2.1-S2.3) from both of *TP53*$^{-/-}$*;PDGFRA*$^{wt/\Delta 8\text{-}9}$ (T) and *PTEN*$^{-/-}$*;NF1*$^{-/-}$ (P) iGBMs were analyzed. Nomenclatures shown in quoted bold characters are used in subsequent panels of this figure. (B) Principal component

analysis of all the sequenced samples. (C) Uniform Manifold Approximation and Projection (UMAP) analysis of all the sequenced samples. (D) GBM subtype analysis based on the average of individual cells in each sample. (E) GBM subtype analysis at single cell resolution. (F) UMAP showing populations with cell-cycle signatures and (G) stemness signatures.

Materials and Methods

Cell culture

Human iPS cells, CV-iPS-B cells (*28*), were cultured on plates coated with Matrigel hESC-Qualified Matrix (Corning) in mTeSR1 media (Stemcell Technologies). NPCs were cultured on Matrigel-coated plates in NPC maintenance media containing DMEM/F12 with GlutaMAX (Thermo Fisher Scientific), 1 x N-2 supplement (Thermo Fisher Scientific), 1 x B-27 supplement (Thermo Fisher Scientific), 50mM ascorbic acid (Tocris), 3μM CHIR99021 (Tocris) and 0.5μM purmorphamine (Tocris). Sphere cells were cultured in suspension in DMEM/F12 with GlutaMAX (Thermo Fisher Scientific) with 1 x B-27 supplement, 20 ng/mL EGF (Stemcell Technologies) and 20 ng/mL bFGF (Stemcell Technologies).

Generation and validation of genetically engineered hiPSC clones

A plasmid, pSpCas9(BB)-2A-GFP or px458, which expresses Cas9-T2A-GFP and sgRNA (*29*), was purchased from Addgene (Plasmid #48138). The designated sgRNA sequences for each of the targeted genes were cloned into px458 using combinations of top and bottom oligonucleotides listed below.
PTEN-intron 4-top: 5'-CACCGGAATTTACGCTATACGGAC-3',
PTEN-intron 4-bottom: 5'-AAACGTCCGTATAGCGTAAATTCC-3',
PTEN-intron 5-top: 5'-CACCGAACAAGATCTGAAGCTCTAC-3',
PTEN-intron 5-bottom: 5'-AAACGTAGAGCTTCAGATCTTGTTC-3',
TP53-intron 1-top: 5'-CACCGGGTTGGAAGTGTCTCATGC-3',
TP53-intron 1-bottom: 5'-AAACGCATGAGACACTTCCAACCC-3',
TP53-intron 6-top: 5'-CACCGCATCTCATGGGGTTATAGGG-3',
TP53-intron 6-bottom: 5'-AAACCCCTATAACCCCATGAGATGC-3',
NF1-intron 31-top: 5'-CACCGATAGCACTCTTCCCGAGCTA-3',
NF1-intron 31-bottom: 5'-AAACTAGCTCGGGAAGAGTGCTATC-3',
NF1-intron 33-top: 5'-CACCGCTTTGGGGAGGTCTTTCGTC-3',
NF1-intron 33-bottom: 5'-AAACGACGAAAGACCTCCCCAAAGC-3',
PDGFRA-intron 7-top: 5'-CACCGATTTGTATGTAGCGGTCTGC-3',
PDGFRA-intron 7-bottom: 5'-AAACGCAGACCGCTACATACAAATC-3',
PDGFRA-intron 9-top: 5'-CACCGCCACGGGAACACTCTAAGA-3',
PDGFRA-intron 9-bottom: 5'-AAACTCTTAGAGTGTTCCCGTGGC-3'.
Each of top and bottom oligonucleotides were phosphorylated and annealed by incubating 10 μM each of oligonucleotides, 1 x T4 DNA ligase buffer (New England Biolabs), 5U T4 polynucleotide kinase (New England Biolabs) at 37ºC for 30 minutes, 95ºC for five minutes and by cooling down to 25ºC at 0.1ºC / second using a thermocycler. Annealed oligonucleotides were cloned into px458 by incubating 25 ng px458, 1uM annealed oligonucleotides, 1 X CutSmart buffer (New England Biolabs), 1 mM ATP (New England Biolabs), 10U BBSI-HF (New England Biolabs) and 200U T4 ligase (New England Biolabs) at 37ºC for 5 minutes, 23ºC for five minutes for 30 cycles. Correct cloning of each sgRNA sequence was confirmed by Sanger sequencing using U6 sequencing primer: 5'-GATACAAGGCTGTTAGAGAGATAATT-3'.
Human iPSCs were cultured in 10 μM Y-27632 RHO/ROCK pathway inhibitor for 2 hours before dissociation. The cells were dissociated to single cells using Accutase (Innovative Cell Technologies). The dissociated hiPSCs (1 x 10^6 cells) were resuspended in 100 μl of supplemented solution of Human Stem Cell Nucleofector Kit 1 (Lonza) containing 8 μg total of

a combination of px458 plasmids targeting each gene and electroporated using B-016 program of Nucleofector 2b (Lonza). Electroporated hiPSCs were cultured on Matrigel-coated plates in mTeSR1 for 48 hours. GFP-positive cells were then sorted by flow cytometer (SH800, SONY) and 1-2 x 10^4 sorted cells were plated on a 10-cm Matrigel-coated plate in mTeSR1. Isolated colonies were manually picked and plated in duplicated Matrigel-coated 96-well plates.
The hiPSCs clones on one of the duplicated 96-well plates were lysed using QuickExtract DNA Extraction Solution (Epicentre) and genotyping PCR was performed using Platinum Taq DNA Polymerase High Fidelity (Thermo Fisher Scientific) in 10-µl reaction volume containing 0.2 µM of each primer with the following reaction conditions: 94ºC for 2 min, 40 cycles of 94ºC for 15 s, 55ºC for 30 s, and 68ºC for 4 min. Primers used for the genotyping PCR were listed below.
PTEN-i4-f: 5'-GAGTCCTGACGAAATGTCCATG-3',
PTEN-i5-r: 5'-CCTGTT TTCCAGGGACTGAG-3',
NF1-i31-f: 5'-ACTCTGGAAAGGGATGGGAG-3',
NF1-i33-r: 5'-CCGGCTTCAGCTTCAAAGTAG-3',
TP53-i1-f: 5'-CCGATCACCTGAAGTAAGGAG-3',
TP53-i6-r: 5'-CCTTAGCCTCTGTAAGCTTCAG-3',
PDGFRA-i7-f: 5'-TGTACTCCTGTCCCCAGCTG-3',
PDGFRA-i9-r: 5'-TCCTGAGAGTCATGGCAATG-3'.
Total RNA was extracted from the edited hiPSCs using RNeasy Plus Mini Kit (Qiagen) and was reverse transcribed using RNA to cDNA EcoDry Premix (Clontech) according to the manufacturer's instruction. Triplicate qPCR reactions containing cDNA obtained from 10ng equivalent RNA were run on a CFX96 Real Time System (Bio-Rad) to confirm designated targeting of the genes with the following reaction conditions: 95ºC for 5 min, 40 cycles of 95ºC for 15 s, 56ºC for 30 s. Primer pairs were designed to span the deleted regions of each target gene. The data was normalized to GAPDH and the relative transcript levels were determined using $2^{-\Delta}$Ct formula. Primers used for the RT-qPCR were listed below.
GAPDH-RT-f: 5'-AATTTGGCTACAGCAACAGGGTGG-3',
GAPDH-RT-r: 5'-TTGATGGTACATGACAAGGTGCGG-3',
PTEN-RT-f: 5'-CGAACTGGTGTAATGATATGT-3',
PTEN-RT-r: 5'-CATGAACTTGTCTTCCCGT-3',
NF1-RT-f: 5'-GCCACCACCTAGAATCGAAAG-3',
NF1-RT-r: 5'-AGCAAGCACATTGCCGTCAC-3',
TP53-RT-f: 5'-CCAAGTCTGTGACTTGCACG-3',
TP53-RT-r: 5'-GTGGAATCAACCCACAGCTG-3',
PDGFRA$^{\Delta 8\text{-}9}$-RT-f: 5'-GATGTGGAAAAGATTCAGGAAATAAGATG-3',
PDGFRA^{wt}-RT-f: 5'-CGCCGCTTCCTGATATTGAG-3',
PDGFRA-RT-r: 5'-CTCCACGGTACTCCTGTCTC-3'.
The qPCR products were visualized by agarose gel electrophoresis.

Differentiation of hiPSCs to neural progenitor cells

Generation of small molecule neural progenitor cells (smNPCs) from iPSCs was adapted from a previous study (*12*). Briefly, human iPSCs at 70%–80% confluency were dissociated using accutase (Innovative Cell Technologies) and resuspended at 1x10^6 cells/ml in N2B27 medium (DMEM/F12 with GlutaMAX (Thermo Fisher Scientific), 1 x N-2 supplement (Thermo Fisher Scientific), 1 x B-27 supplement (Thermo Fisher Scientific), 150 mM ascorbic acid (Tocris), and 1% Penicillin/Streptomycin) supplemented with 1 µM Dorsomorphin (Tocris), 10 µM SB431542

(Tocris), 3 μM CHIR99021, 0.5 μM Purmorphamine and 5 mM Y-26732 (Stemcell Technologies). Three million cells were transferred into one well of an uncoated 6-well tissue culture plate and incubated at 37ºC, 5% CO2 on a shaker at 90 rpm. Uniform small EBs formed within 24h and increased in size over the following days. After 48h, a full media change was performed with N2B27 medium supplemented with Dorsomorphin, SB431542, CHIR99021, and Purmorphamine. At this time, about 2/3 of EBs were either discarded or EBs were split across 3 wells of a 6-well plate to reduce the high cell density required initially to ensure uniform formation of embryoid bodies. On days 3-5, half media change was performed with fresh N2B27 media supplemented with Dorsomorphin, SB431542, CHIR99021, and Purmorphamine. On day 6, Dorsomorphin and SB431542 were withdrawn and a full media change with smNPC media (N2B27 media supplemented with 3 μM CHIR99021 and 0.5 μM Purmorphamine) was performed. At this stage, neuroepithelial folds were clearly visible in all EBs. On day 8, EBs were triturated by pipetting 10-15 times with a P1000 pipette and plated onto matrigel-coated 10 cm plates. After 3-4 days, attached EB fragments and outgrown cells were dissociated to single cells with accutase (Innovative Cell Technologies) and split at a 1:6 to 1:8 ratio onto matrigel-coated plates. After the first passage, cells were passaged at a 1:10 to 1:15 ratio every 3-6 days. For the first few passages, large flat non-smNPCs could be observed between smNPC colonies, but progressively disappeared no later than passages 3-6 in almost all cell lines. Total RNA was extracted from the differentiated smNPCs using RNeasy Plus Mini Kit and was reverse transcribed using RNA to cDNA EcoDry Premix according to the manufacturer's instruction. Triplicate qPCR reactions containing cDNA obtained from 10 ng equivalent RNA were run on a CFX96 Real Time System to confirm NPC differentiation with the following reaction conditions: 95ºC for 5 min, 40 cycles of 95ºC for 15 s, 56ºC for 30 s. The data was normalized to GAPDH and the relative transcript levels were determined using $2^{-\Delta}$Ct formula. Primers used for the RT-qPCR were listed below.

Nanog-RT-f: 5'-GAAATACCTCAGCCTCCAGC-3',
Nanog-RT-r: 5'-GCGTCACACCATTGCTATTC-3',
Oct4-RT-f: 5'-AGAACATGTGTAAGCTGCGG-3',
Oct4-RT-r: 5'-GTTGCCTCTCACTCGGTTC-3',
Nestin-RT-f: 5'-GGTCTCTTTTCTCTTCCGTCC-3',
Nestin-RT-r: 5'-CTCCCACATCTGAAACGACTC-3',
Pax6-RT-f: 5'-GCCCTCACAAACACCTACAG-3',
Pax6-RT-r: 5'-TCATAACTCCGCCCATTCAC-3',
Sox1-RT-f: 5'-CAGCAGTGTCGCTCCAATCA-3',
Sox1-RT-r: 5'-GCCAAGCACCGAATTCACAG-3'.

Spontaneous differentiation of NPCs was performed by maintaining NPCs on matrigel-coated plates in DMEM supplemented with 10% FBS for a week.

Immunofluorescence microscopy

Cells were plated on poly-D-lysine-coated glass coverslips (Thermo Scientific), fixed with 10% formalin (Sigma-Aldrich), blocked with 2% of BSA IgG-free (Jackson ImmunoResearch) and stained with primary antibodies to GFAP (BD Bioscience), Olig2 (Sigma-Aldrich), and Tuj1 (Covance) overnight at 4ºC. Secondary antibody was added for 1 h at room temperature. Coverslips were mounted on microscope glass slides using Fluro-Gel with DAPI (Electron Microscopy Science) followed by visualization using a fluorescent microscope (Keyence).

Intracranial tumor formation

Animal research experiments were conducted under the regulations of the UCSD Animal Care Program, protocol number S00192M. Wildtype and edited smNPCs were dissociated using accutase (Innovative Cell Technologies), washed with PBS, and resuspended at $1x10^6$ cells in 2µL PBS supplemented with 0.1% BSA per animal. Resuspended cells were kept on ice and were inoculated into the striatum of 4-6 week-old female Nod/Scid mice (Charles River Laboratory) by stereotactic injections (1.0 mm anterior and 2.0 mm right to the bregma, and 3mm deep from the inner plate of the skull). Wildtype hiPSCs were injected as a control as well.

Immunohistochemistry

Paraffin-embedded tissue blocks were sectioned using the UCSD Moore's Cancer Center Pathology Core and the Center for Advanced Laboratory Medicine (UCSD). Paraffin-embedded tissue sections underwent immunohistochemical analysis using primary antibodies to GFAP (BD Bioscience), Ki-67 (Abcam), and human nuclear antigen, NM95 (Abcam).

Sphere cell culture of induced glioblastoma

Tumors were excised from mouse brains and cut in small pieces using a scalpel, and then incubated in 3.6 ml of Hank's Balanced Salt Solution (HBSS, Sigma) with 0.4 ml of 10x Trypsin solution (Sigma) at 37ºC for 20 min. After incubation, 200 µl of 10 mg/ml DNaseI stock solution (Sigma) was added and incubated for 60 seconds, and then 6 ml of HBSS was added to neutralize Trypsin and DNaseI. Tumor tissue was resuspended by pipetting up and down several times through a glass Pasteur pipette. Dissociated tissue was filtered through a strainer and was spun down by centrifugation at 400G for 3 min. Cells were resuspended in 1 ml of PBS and 9 ml of ACK lysing buffer (Invitrogen) and were incubated at 37 ºC for 10 min to remove red blood cells. Approximately $1x10^6$ cells were resuspended in 100 µl of MACS/BSA buffer (Miltenyi Biotec) and were incubated with 2 µl of Fc blocking solution (BioLegend) for 5 min on ice. After blocking, 5 µl of PE-conjugated anti-human HLA-A,B,C antibody (BioLegend) was added and cells were incubated for 15 min on ice. Stained cells were washed twice with 500µl of MACS/BSA buffer. PE-positive cells were then sorted using a flow cytometer (SH800, SONY). Sorted human iGBM cells were maintained in DMEM/F12 with GlutaMAX (Thermo Fisher Scientific) with 1 x B-27 supplement (Thermo Fisher Scientific), 20 ng/mL EGF (Stemcell Technologies) and 20 ng/mL bFGF (Stemcell Technologies).

Extreme Limiting dilution assay

Extreme limiting dilution assay was performed as described (*15*). NPCs and iGBM spheres were dissociated into single cells using accutase (Innovative Cell Technologies) and 1, 5, 10, 20, 50 and 100 cells/well were plated in 96-well plates with five replicates for each experimental condition. The total number of spheres, per well and per treatment, were quantified after 14 days in culture. Data was analyzed by extreme limiting dilution analysis (http://bioinf.wehi.edu.au/software/elda/).

Secondary tumor models and temozolomide treatment

Animal research experiments were conducted under the regulations of the UCSD Animal Care Program, protocol number S00192M. Primary iGBM spheres were dissociated using accutase (Innovative Cell Technologies), washed with PBS, and resuspended at $2.5x10^5$ cells in 2µL PBS supplemented with 0.1% BSA per animal. Resuspended cells were kept on ice and were

inoculated into the striatum of 4-6 week-old female Nod/Scid mice (Charles River Laboratory) by stereotactic injections (1.0 mm anterior and 2.0 mm right to the bregma, and 3mm deep from the inner plate of the skull). Treatment of the mice started 7 days after inoculation of the iGBM cells by intraperitoneal injection of either vehicle (DMSO) or 50 mg/kg of temozolomide (Selleckchem). The mice were treated once daily for the first 3 days followed by 2-day drug holidays, and then once daily for 2 days again followed by 2-day drug holidays and another set of 2-day once daily treatment. This set of treatment was repeated every 4 weeks and percentage of surviving mice over time was recorded. RT-qPCR to evaluate MGMT expression was run on a CFX96 Real Time System to confirm differentiation to NPCs with the following reaction conditions: 95ºC for 5 min, 40 cycles of 95ºC for 15 s, 56ºC for 30 s. The data was normalized to GAPDH and the relative transcript levels were determined using $2^{-\Delta}$Ct formula. Primers used for the RT-qPCR were listed below.
MGMT-RT-f: 5'-GCTGAATGCCTATTTCCACCA-3',
MGMT-RT-r: 5'-CACAACCTTCAGCAGCTTCCA-3',

Cytogenetics

Metaphase cells were obtained by treating cells with Karyomax (Gibco) at a final concentration of 0.1 µg/ml for 1-3 hours. Cells were collected, washed in PBS, and resuspended in 0.075M KCl for 15-30 minutes. Carnoys fixative (3:1 methanol/glacial acetic acid) was added dropwise to stop the reaction. Cells were washed an additional 3 times with Carnoys fixative, before being dropped onto humidified glass slides for metaphase cell preparations. DAPI was added to the slides. Images were captured with an Olympus FV1000 confocal microscope.
Spectral karyotyping analysis was performed at Applied Spectral Imaging.
Genomic DNA extracted from NPCs and iGBM cells using DNeasy blood and tissue kit (Qiagen) was analyzed by digital karyotyping using Illumina HiScan system (Illumina).
To detect DNA replication, cells were labeled with EdU and detected using the Click-iT Plus EdU Alexa Fluor 594 imaging kit (Invitrogen). Briefly, cells were pulse labeled with EdU (10 uM) for 1 hour, then allowed to progress to metaphase for 12 hours. KaryoMax (0.1 ug/ml) was added for 3 hours to arrest cells in metaphase. The cells were then collected and metaphase spreads were prepared (*23*). Cells in metaphase were dropped onto a glass slide, and EdU was detected by applying the Click-iT reaction cocktail directly onto the slides for 20 minutes at room temperature. Slides were then washed with 2X SSC and mounted with anti-fade mounting medium containing DAPI. Cells in metaphase were imaged using an Olympus BX43 fluorescent microscope equipped with a QIClick camera.

Single cell RNA sequencing and analysis

For the single cell RNA sequencing of secondary tumor cells, the tumors were dissected from mouse brains, cut into small pieces, and then incubated in HBSS (Sigma) containing 1x trypsin (Sigma) at 37° for 20 minutes, followed by mechanical dissociation using glass pipettes to obtain single cells. Cultured sphere cells were dissociated using accutase (Innovative Cell Technologies). Single cells were processed through the Chromium Single Cell Gene Expression Solution using the Chromium Single Cell 3' Gel Bead, Chip and Library Kits v2 (10X Genomics) as per the manufacturer's protocol. In brief, single cells were resuspended in 0.04% BSA in PBS. Ten thousand total cells were added to each channel with an average recovery of 3,040 cells. The cells were then partitioned into Gel Beads in Emulsion in the Chromium instrument, where cell lysis and barcoded reverse transcription of RNA occurred, followed by

amplification, shearing and 5′ adaptor and sample index attachment. Agilent High Sensitivity D5000 ScreenTape Assay (Aglient Technologies) was performed for QC of the libraries. Libraries were sequenced on an Illumina NovaSeq. De-multiplexing, alignment to the hg19 transcriptome and unique molecular identifier (UMI)-collapsing were performed using the Cellranger toolkit (version 2.0.1) provided by 10X Genomics. A total of 42,558 cells with approximately 53,000 mapped reads per cell were processed. Analysis of output digital gene expression matrices was performed using the Scanpy v1.3.3 package (*30*). Matrices for all samples were concatenated and all genes that were not detected in at least 20 single cells were discarded, leaving 20,521 genes for further analyses. Cells with fewer than 600 or more than 8,000 expressed genes as well as cells with more than 80,000 UMIs or 0.1% mitochondrial expressed genes were removed from the analysis. Data were log normalized and scaled to 10,000 transcripts per cell. Top 4,000 variable genes were identified with the filter_genes_dispersion function, flavor='cell_ranger'. PCA was carried out, and the top 25 principal components were retained. With these principal components, UMAP was applied. Single cell and mean expression per sample heatmaps were generated with the pl.heatmap and pl.matrixplot functions, respectively. Mean expression levels for the different gene marker sets were obtained by calculating the fraction of known marker genes found per single cell in each sample and setting the sample mean to 1.

RNA sequencing

Total RNA was assessed for quality using an Agilent Tapestation, and all samples had RNA Integrity Numbers above 9.0. RNA libraries were generated using llumina's TruSeq Stranded mRNA Sample Prep Kit (Illumina) following manufacturer's instructions. RNA-seq reads were aligned to the human genome (hg19) with STAR 2.4.0h (outFilterMultimapNmax 20, outFilterMismatchNmax 999, outFilterMismatchNoverLmax 0.04, outFilterIntronMotifs RemoveNoncanonicalUnannotated, outSJfilterOverhangMin 6 6 6 6, seedSearchStartLmax 20, alignSJDBoverhangMin 1) using a gene database constructed from Gencode v19 (*31, 32*). Reads that overlap with exon coordinates were counted using HTSeqcount (-s reverse -a 0 -t exon -i gene_id -m union) (*33, 34*). Raw read counts were processed with DESeq2 (*35*) and only genes with mean read count over 20 were considered for the analysis. Raw read counts were transformed using the variance stabilizing transformation function included in DESeq2 (*36*). Mean and standard deviation of normalized expression were calculated for each gene and Z-scores were determined by subtracting the mean from each expression value and dividing by the standard deviation.

Statistical analyses

All statistical analyses were performed using GraphPad Prism 6 software. Data are representative of results obtained in at least 3 independent experiments. Data sets were analyzed by unpaired t-test to determine significance ($p<0.05$). Kaplan–Meier curves and comparison of survival were analyzed using Long-rank (Mantel–Cox) test.

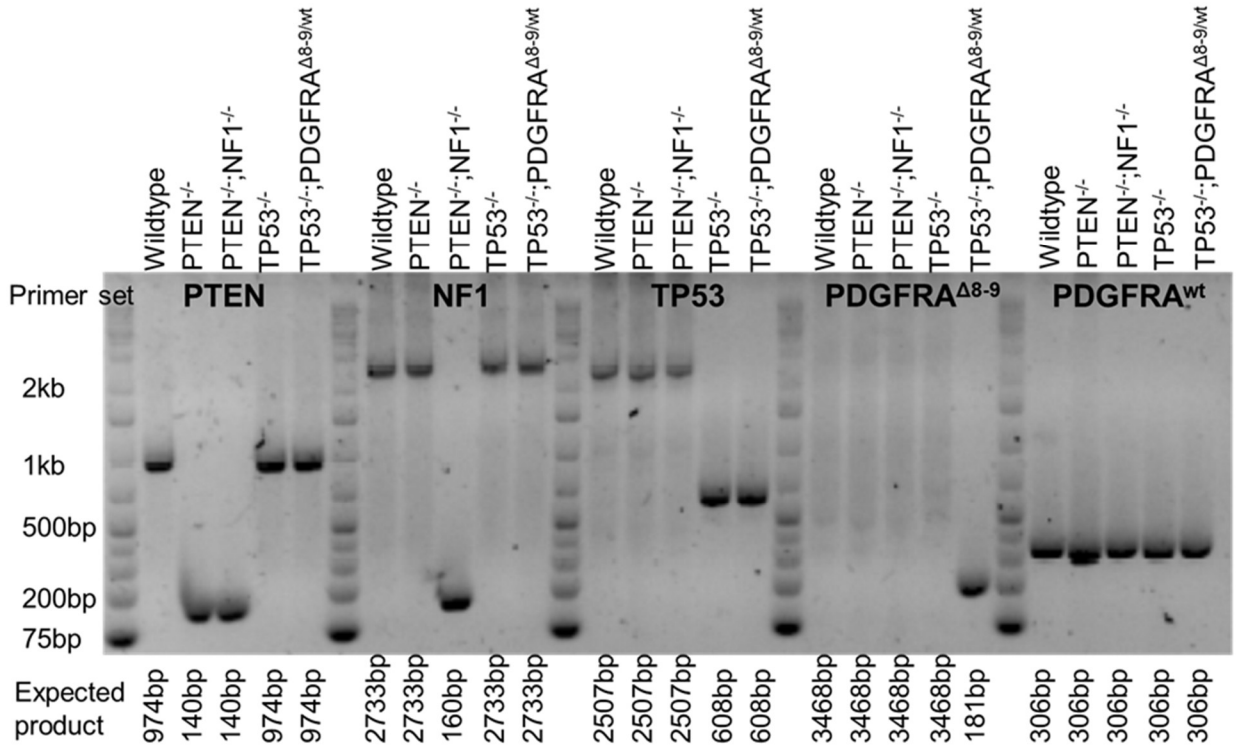

Fig. S1.

Genotyping PCR of edited hiPSCs. Agarose gel electrophoresis of genotyping PCR for each gene in edited hiPSC clones. PCR amplicons from targeted alleles were expected to be 140, 160, 608, and 181 base pairs for *PTEN*, *NF1*, *TP53*, and *PDGFRA*, respectively.

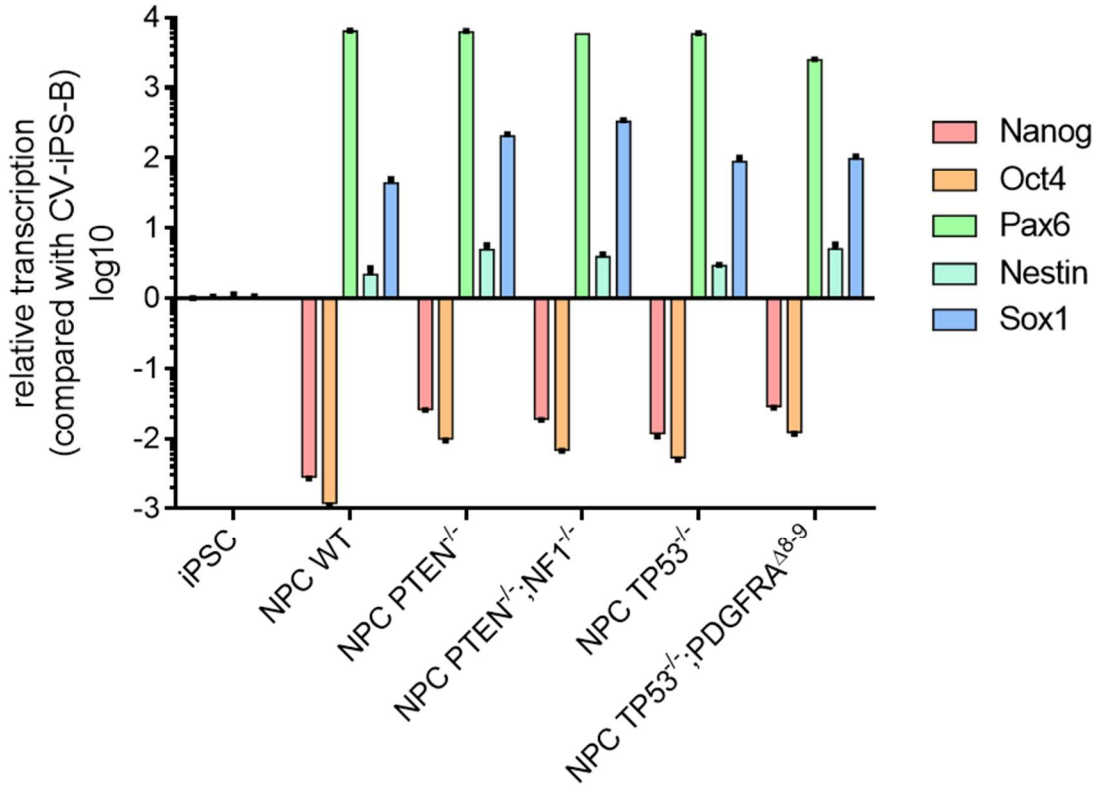

Fig. S2.

Expression of pluripotency markers and neural progenitor markers in different NPC clones. Relative transcript levels of pluripotency markers, Nanog, and Oct4, and neural progenitor markers, Pax6, Nestin, and Sox1, normalized to internal control, GAPDH. The relative transcript levels for each NPC clone was compared to wildtype hiPSCs.

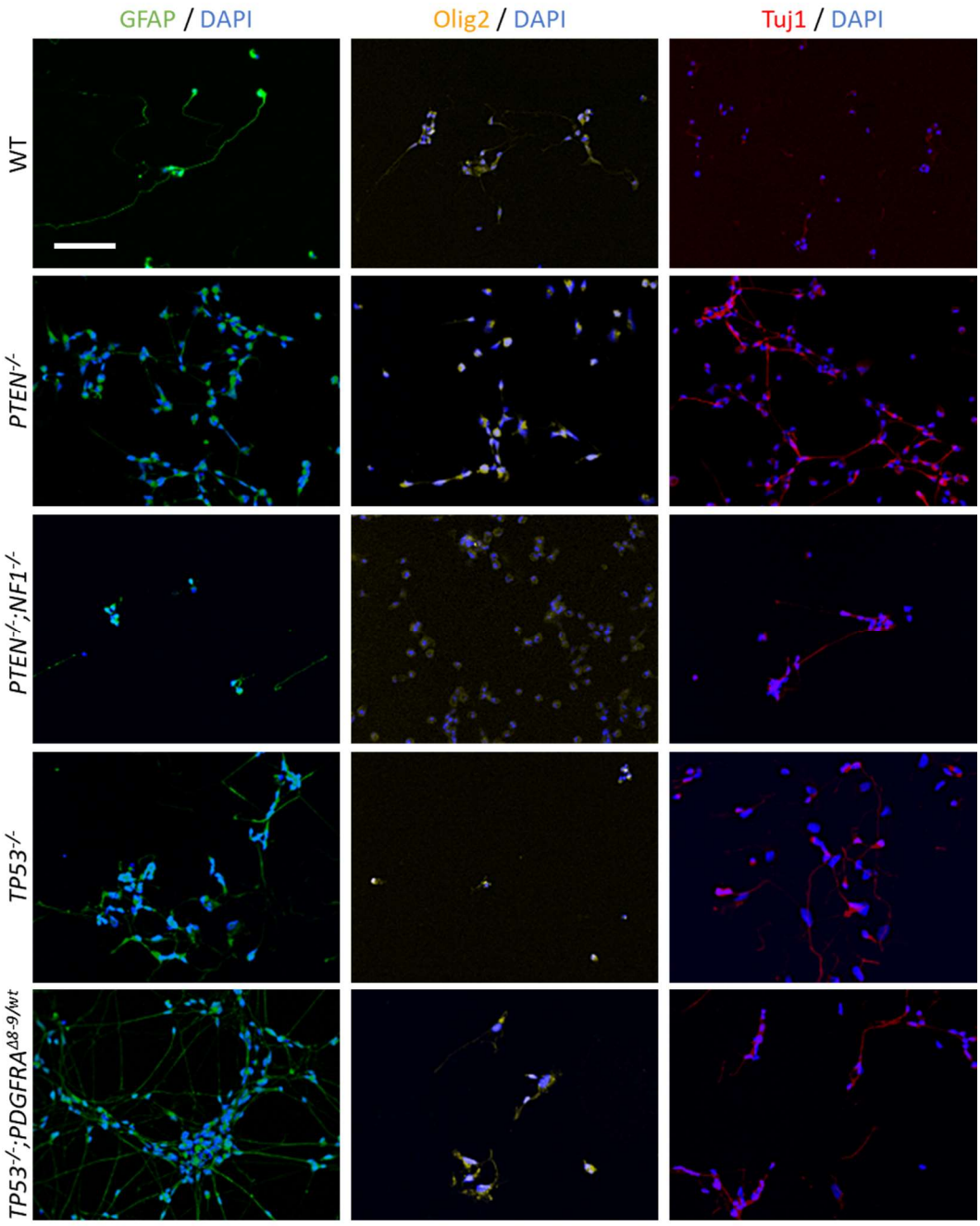

Fig. S3.

NPCs with different genetic modifications retain neural and glial lineage differentiation capacity. Immunocytochemistry for astrocyte marker, GFAP, oligodendrocyte marker, Olig2, neuron maker, Tuj1, after directed differentiation of different NPC clones.

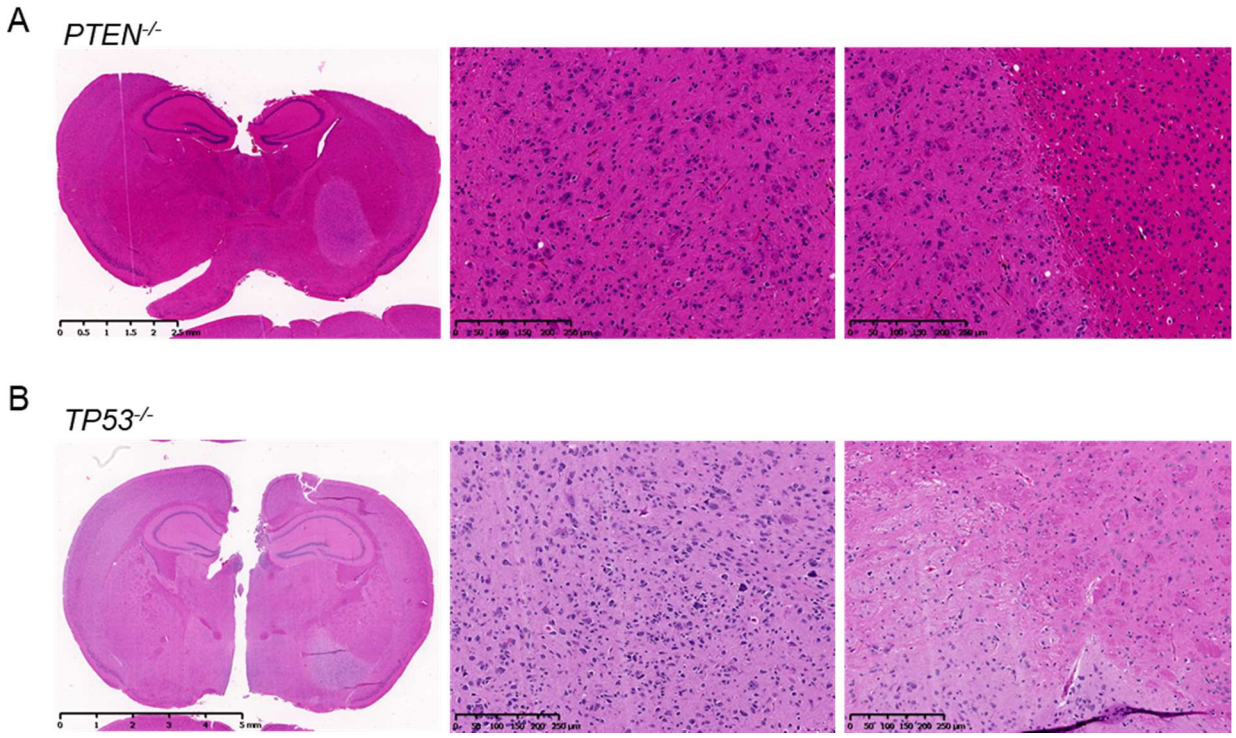

Fig. S4

***PTEN*$^{-/-}$ and *TP53*$^{-/-}$ singly edited NPCs do not give rise to tumors.** (A) Hematoxylin and eosin staining of mouse brain 9 months after injection of *PTEN*$^{-/-}$ NPCs. (B) Hematoxylin and eosin staining of the brain 9 months after injection of *TP53*$^{-/-}$ NPCs.

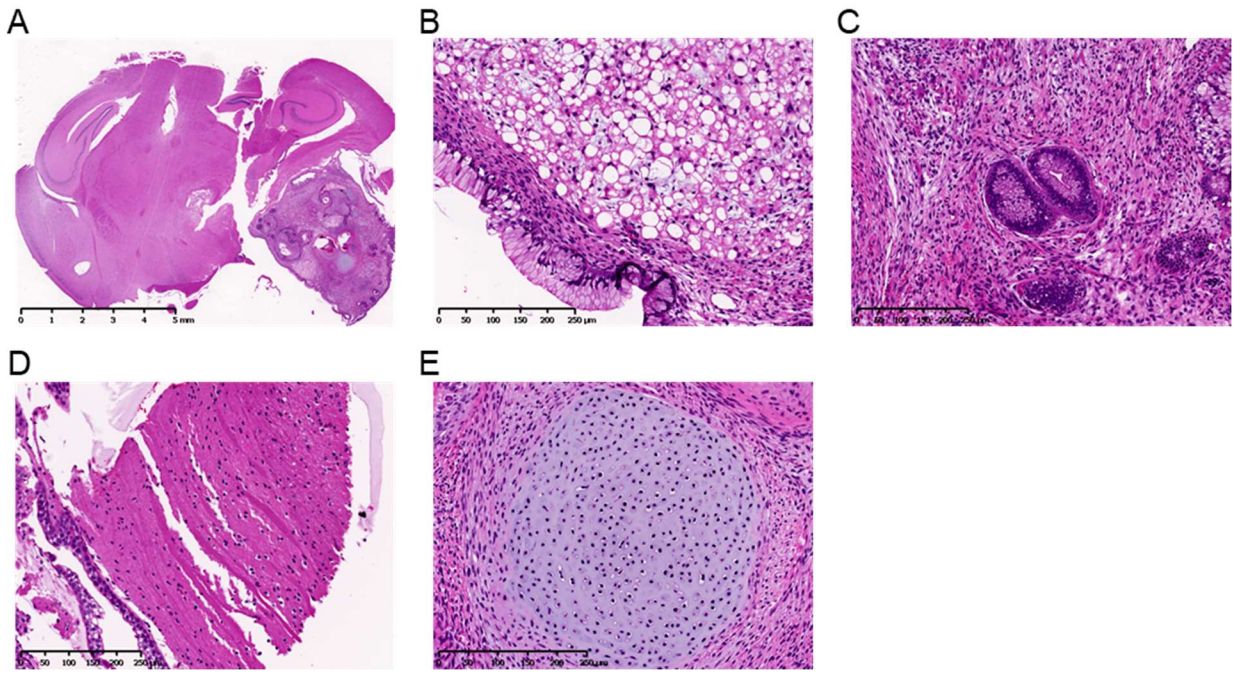

Fig. S5

Wildtype hiPSCs form teratoma-like tumors in the mouse brain. (A) Hematoxylin and eosin staining of mouse brain post-injection of wildtype hiPSCs. (B-E) Hematoxylin and eosin staining of tumors. (B) Adipose tissue-like, (C) gastrointestinal tract-like, (D) muscle-like, and (E) cartilage-like tissues are observed.

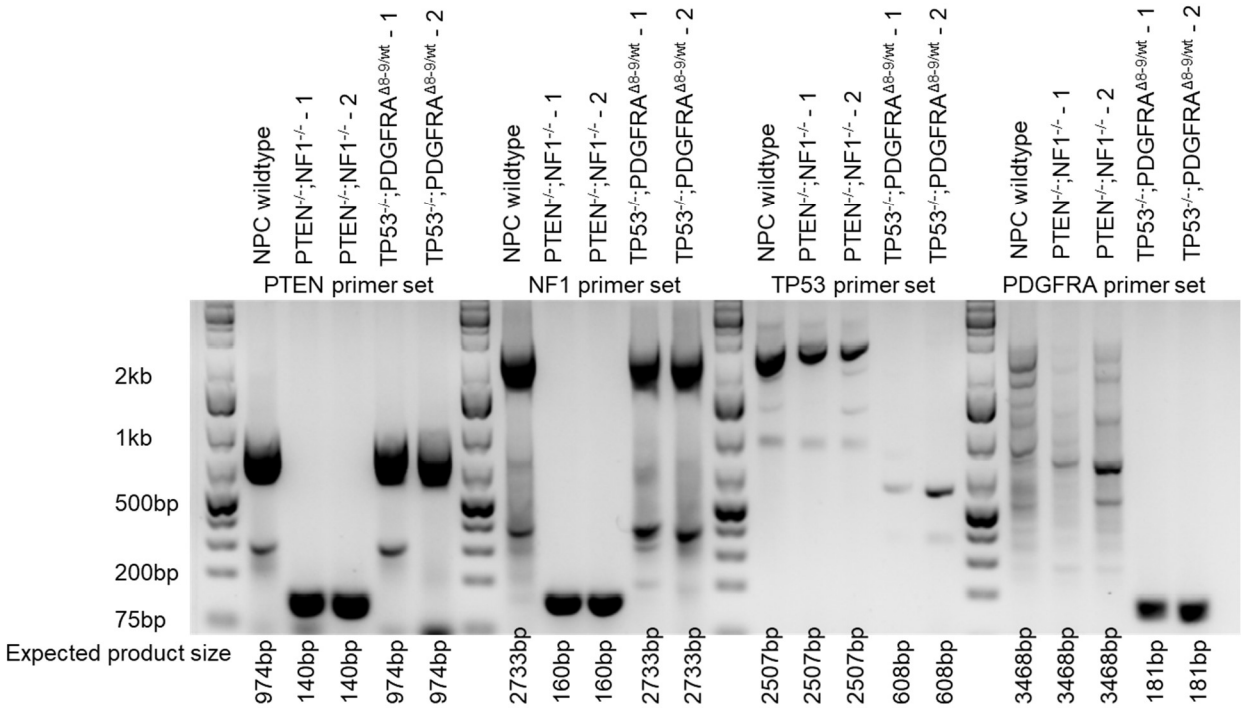

Fig. S6

iGBM samples have the same genotype as pre-engraftment NPCs. Agarose gel electrophoresis of amplicons from genotyping PCR for each gene in iGBM samples. PCR amplicons from targeted alleles were expected to be 140, 160, 608, and 181 bases for *PTEN*, *NF1*, *TP53*, and *PDGFRA*, respectively.

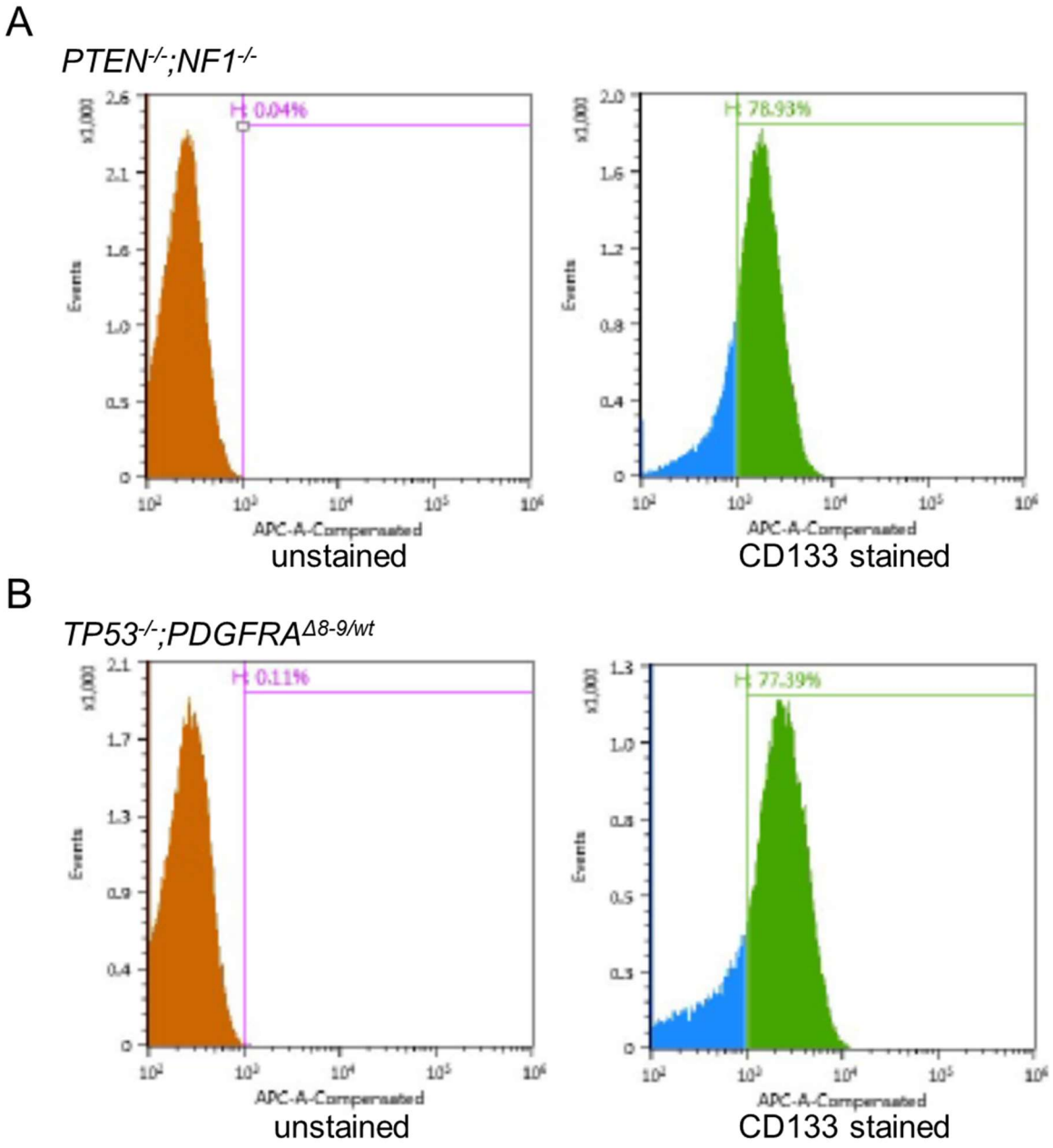

Fig. S7
Input NPCs are homogeneously positive for CD133. CD133 staining of (A) *PTEN*$^{-/-}$;*NF1*$^{-/-}$,and (B) *TP53*$^{-/-}$;*PDGFRA*$^{wt/\Delta 8\text{-}9}$ NPCs analyzed by flow cytometry.

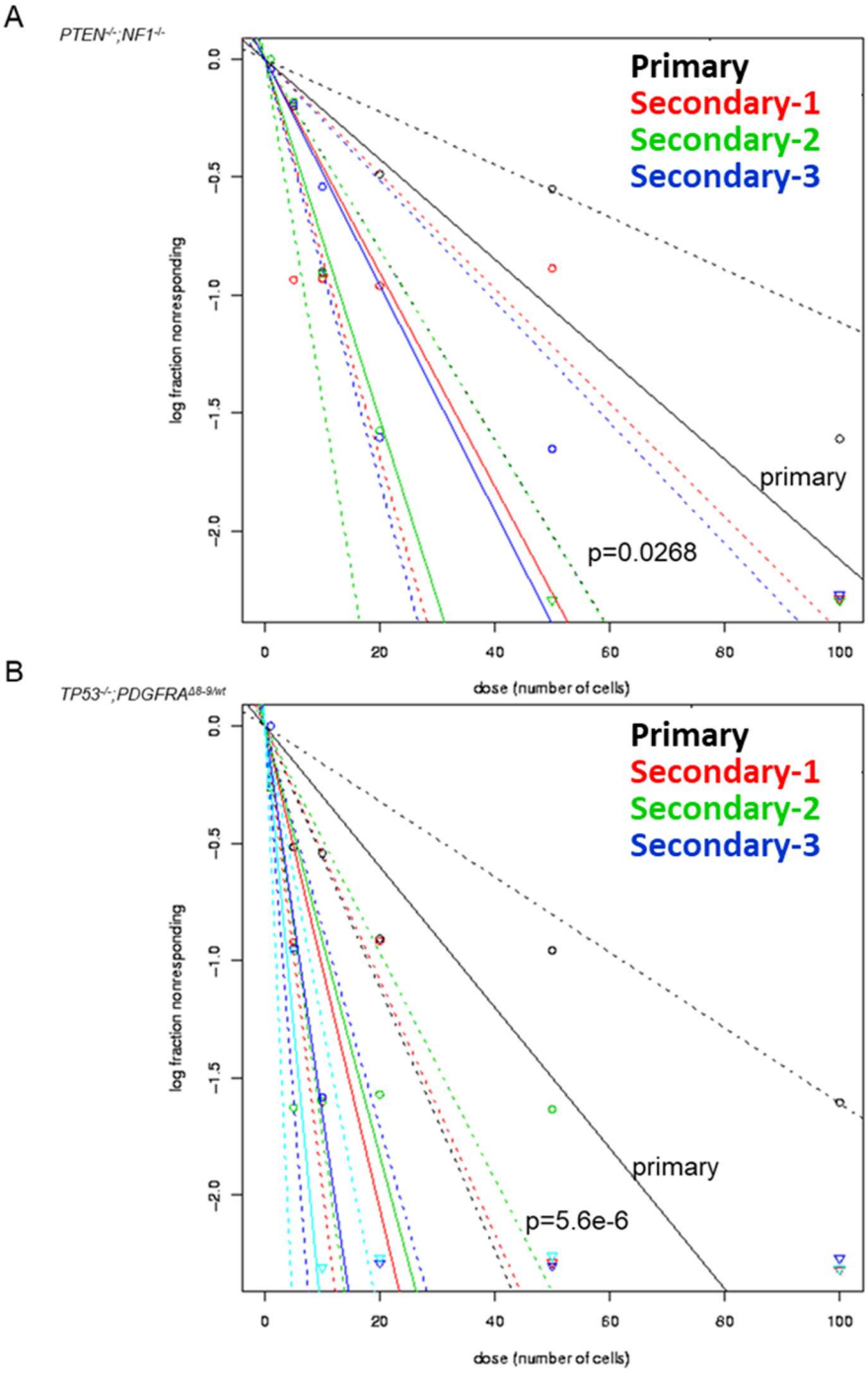

Fig. S8

Secondary iGBM sphere cells possess greater self-renewal capabilities compared with primary iGBM sphere cells. Extreme limiting dilution analysis of primary and secondary sphere cells obtained from (A) *PTEN*$^{-/-}$;*NF1*$^{-/-}$,and (B) *TP53*$^{-/-}$;*PDGFRA*$^{wt/\Delta 8\text{-}9}$ iGBMs.

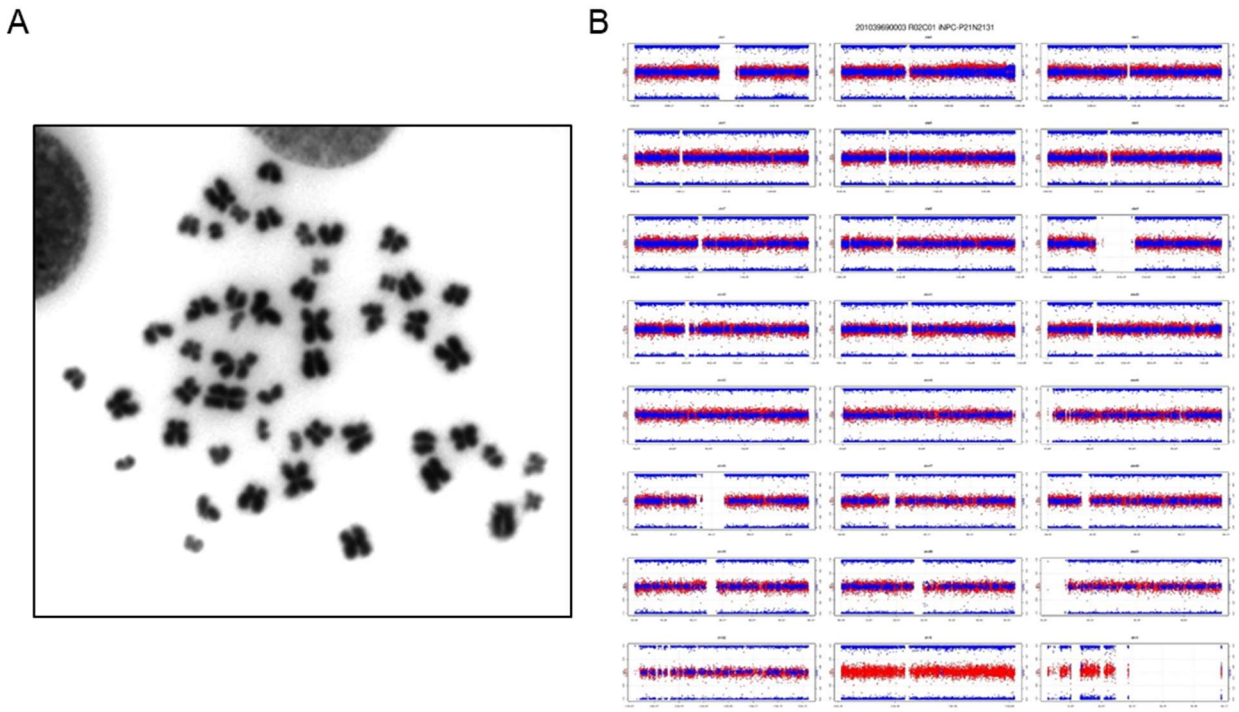

Fig. S9
***PTEN*$^{-/-}$*;NF1*$^{-/-}$ NPCs have normal karyotype.** (A) DAPI staining of metaphase spread of *PTEN*$^{-/-}$*;NF1*$^{-/-}$ NPCs, (B) Digital karyotyping results of *PTEN*$^{-/-}$*;NF1*$^{-/-}$ NPCs.

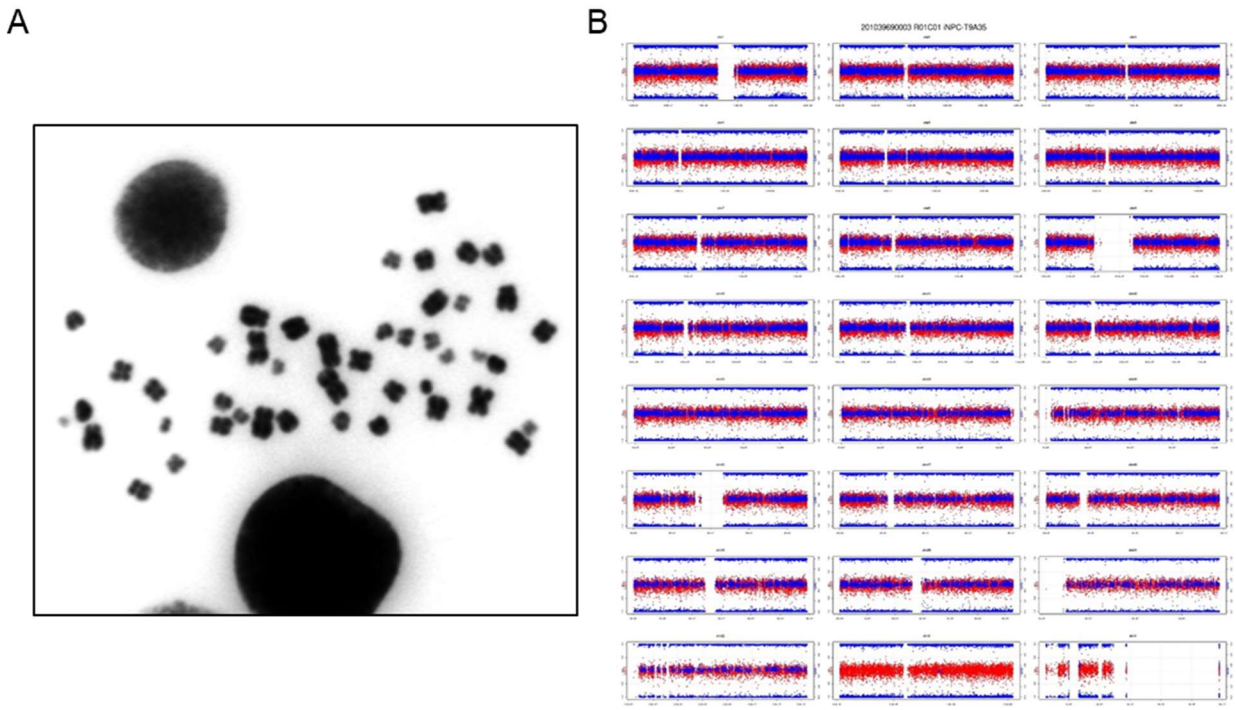

Fig. S10

***TP53*$^{-/-}$*;PDGFRA*$^{wt/\Delta 8\text{-}9}$ NPCs have normal karyotype.** (A) DAPI staining of metaphase spread of *TP53*$^{-/-}$*;PDGFRA*$^{wt/\Delta 8\text{-}9}$ NPCs (B) Digital karyotyping results of *TP53*$^{-/-}$*;PDGFRA*$^{wt/\Delta 8\text{-}9}$ NPCs.

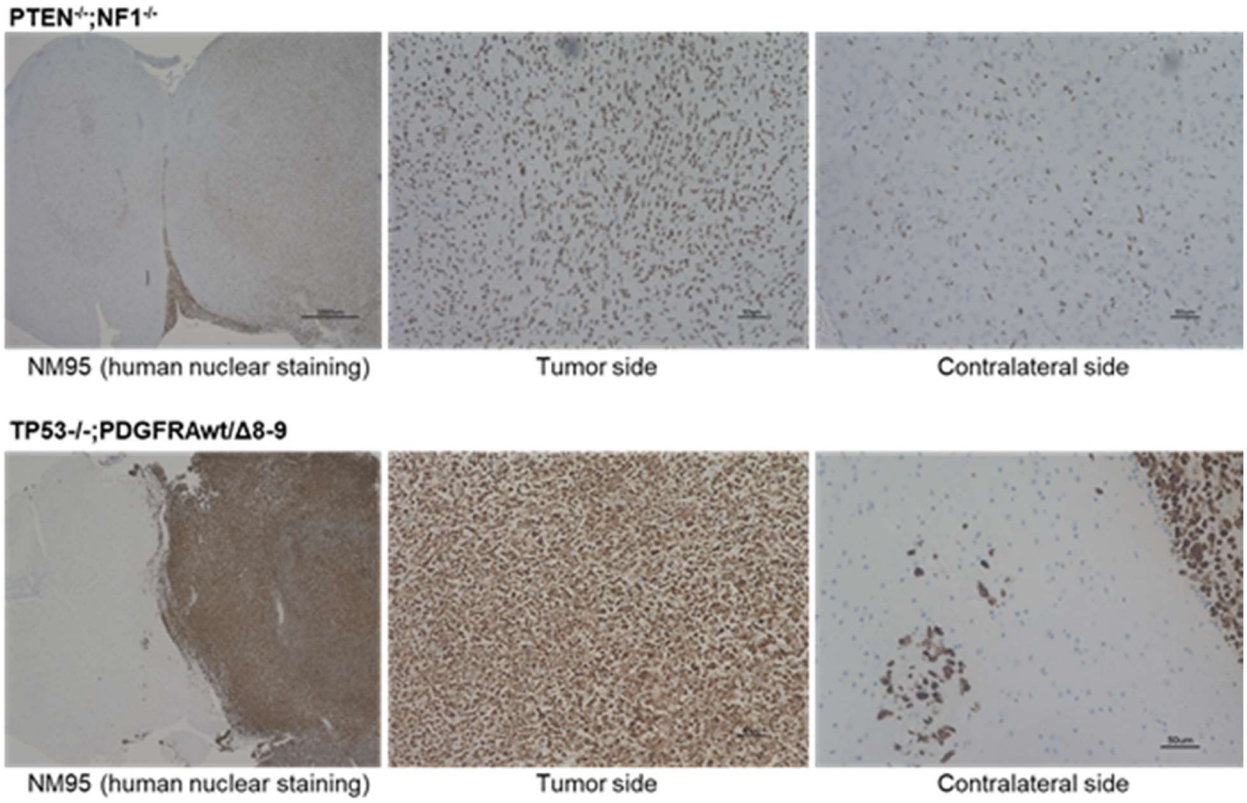

Fig. S11
***PTEN*$^{-/-}$*;NF1*$^{-/-}$ and *TP53*$^{-/-}$*;PDGFRA*$^{wt/\Delta 8\text{-}9}$ iGBMs possess different invasive phenotypes.**
NM95 human nuclear antibody staining of mouse brains with each iGBM tumor.

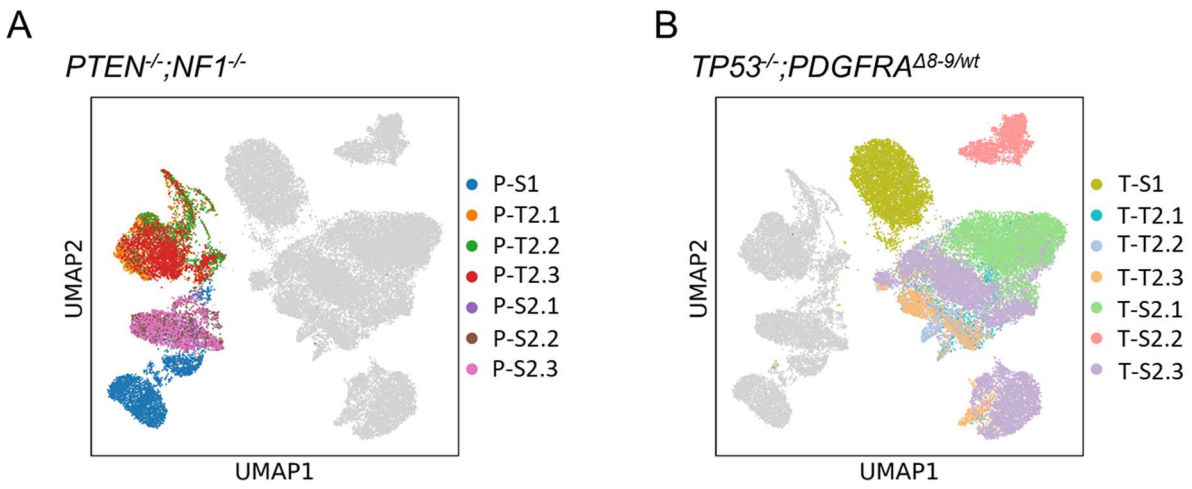

Fig. S12

iGBMs display greatest diversity between different genotypes. Uniform Manifold Approximation and Projection (UMAP) analysis highlighting the samples of different genotypes, **(A) *PTEN*$^{-/-}$;*NF1*$^{-/-}$ and (B) *TP53*$^{-/-}$;*PDGFRA*$^{wt/\Delta 8\text{-}9}$.**

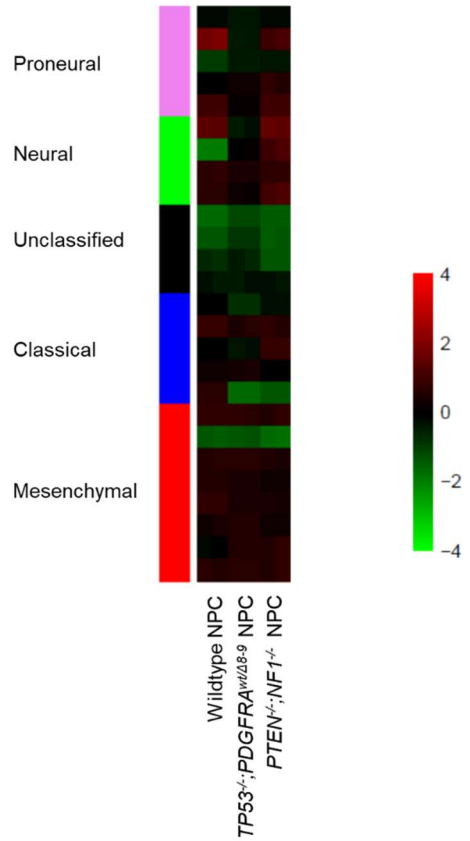

Fig. S13

NPCs with different genetic modifications lack GBM subtype specific signatures that are observed in each corresponding iGBM. Heatmap for GBM subtype gene transcript levels of wildtype, *TP53*$^{-/-}$*;PDGFRA*$^{wt/\Delta 8\text{-}9}$, and *PTEN*$^{-/-}$*;NF1*$^{-/-}$ NPCs.

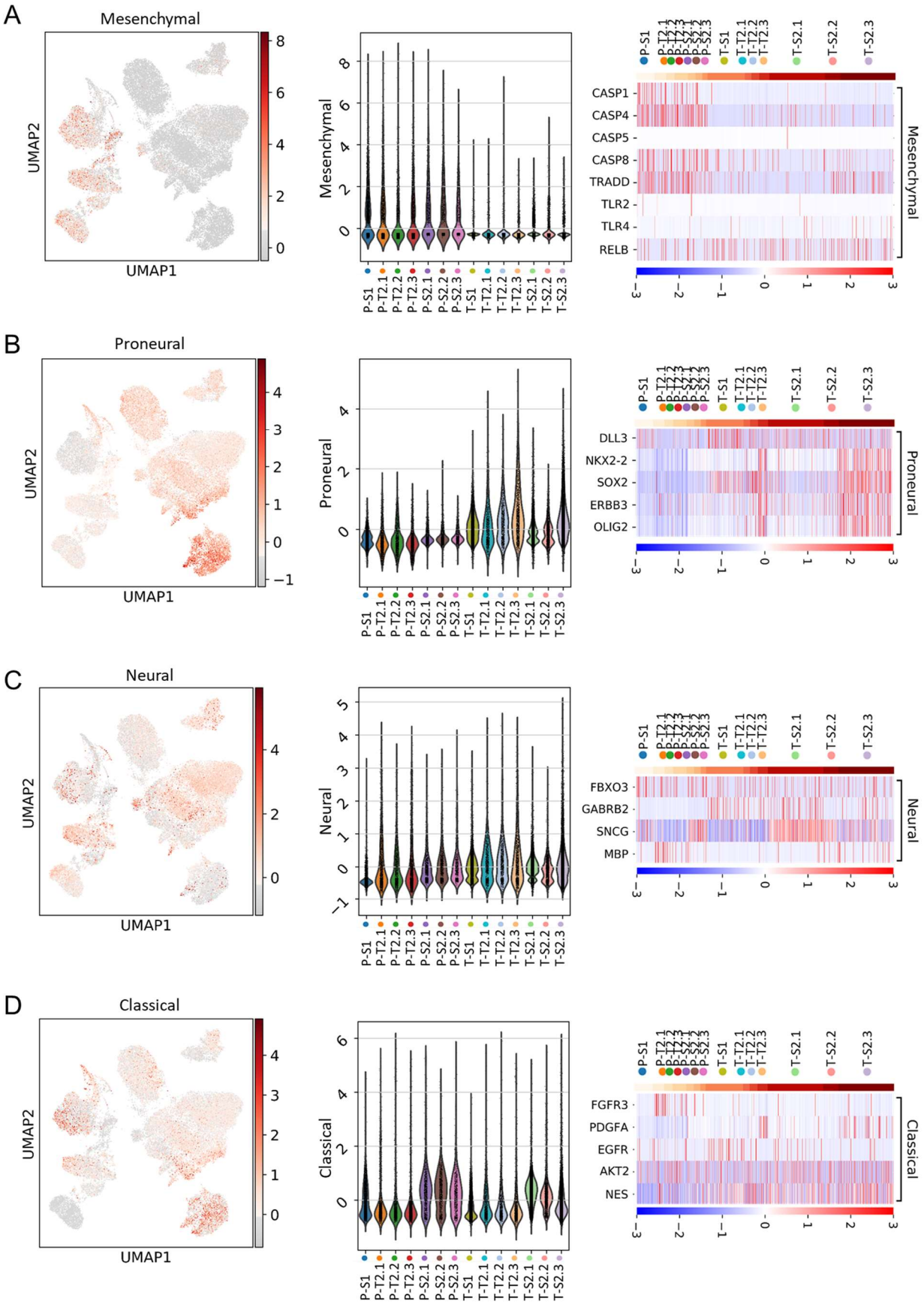

Fig. S14

iGBM samples present intra-tumor heterogeneity with subpopulations of different GBM subtypes, while mesenchymal and proneural populations are enriched in *PTEN*$^{-/-}$;*NF1*$^{-/-}$ and *TP53*$^{-/-}$;*PDGFRA*$^{wt/\Delta 8\text{-}9}$ iGBMs, respectively. Uniform Manifold Approximation and Projection (UMAP) analysis, violin plots, and heatmaps showing expression of genes of (A) mesenchymal, (B) proneural, (C) neural, and (D) classical subtypes.

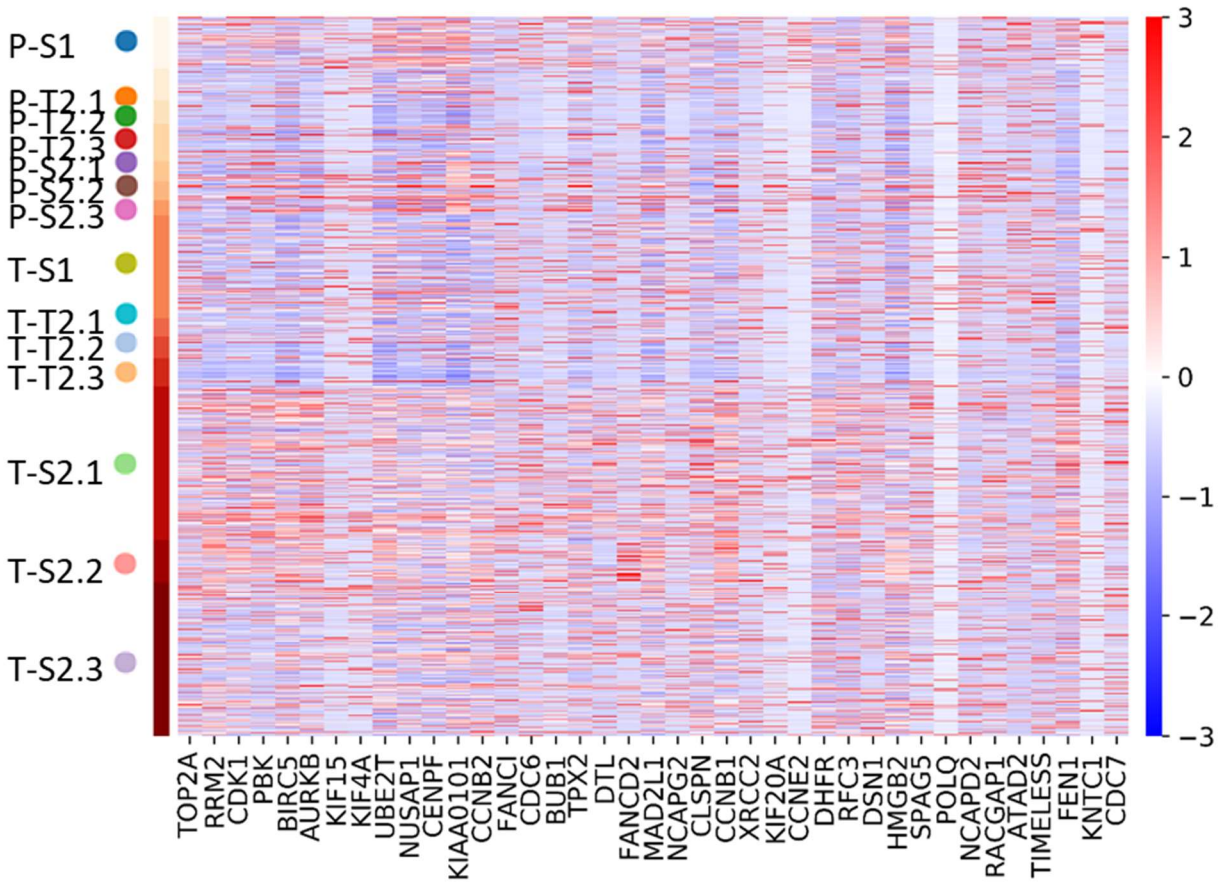

Fig. S15

Subpopulations with GBM cell cycling signatures reside in iGBM samples. A heatmap of expression of GBM cell cycling signature genes.

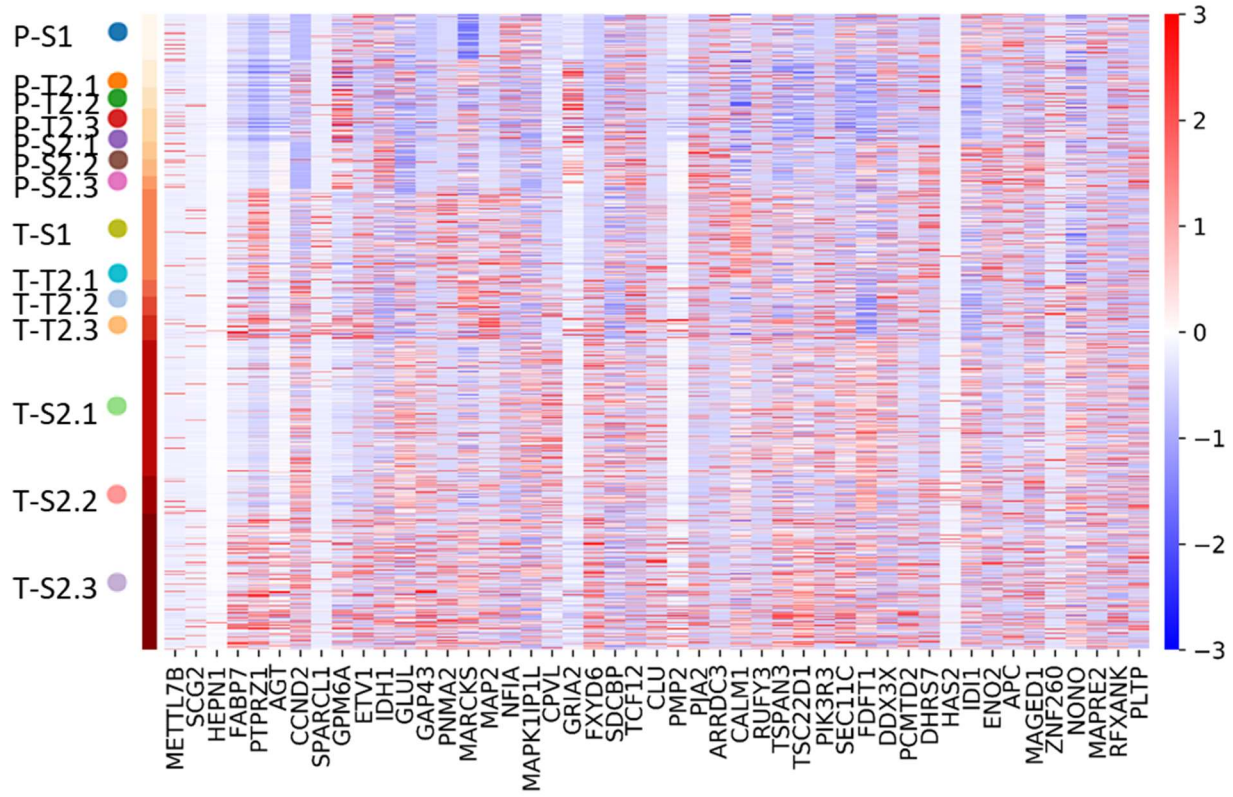

Fig. S16
Subpopulations with GBM stemness signatures reside in iGBM samples. A heatmap of expression of GBM stemness signature genes.

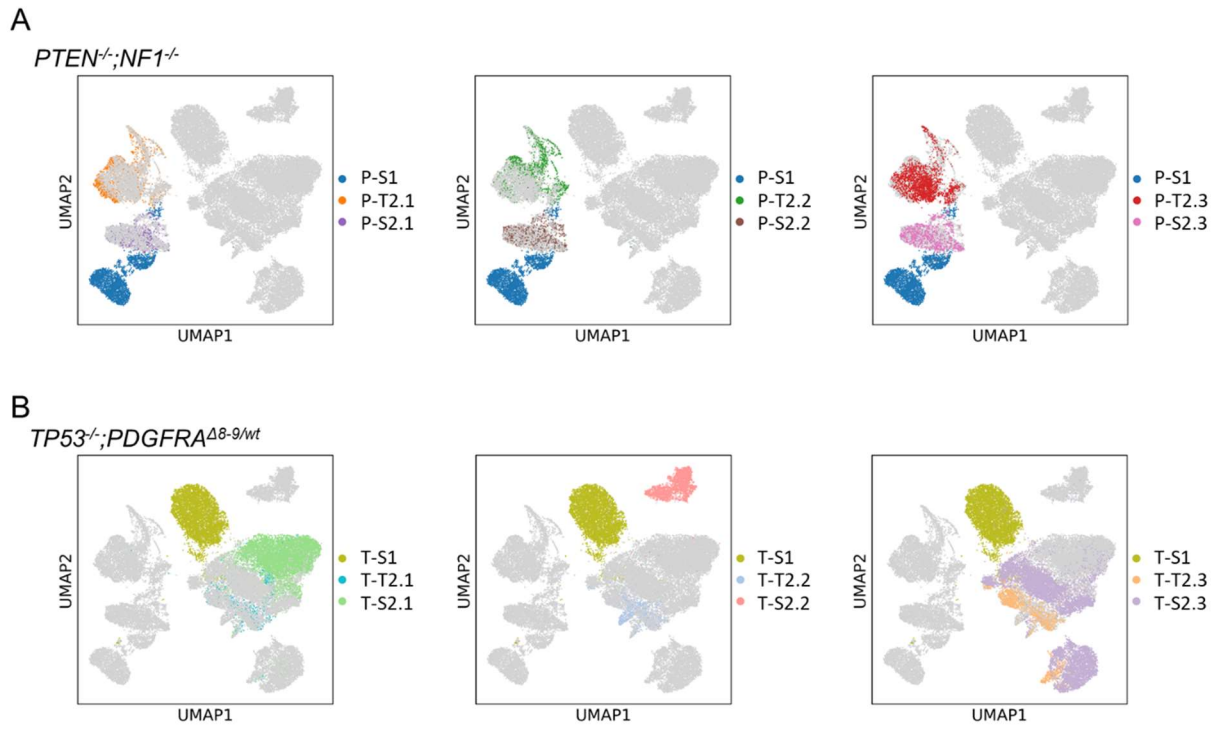

Fig. S17

***TP53*$^{-/-}$*;PDGFRA*$^{wt/\Delta 8\text{-}9}$ iGBMs display more diversities among different passages or replicates compared with *PTEN*$^{-/-}$*;NF1*$^{-/-}$ iGBMs.** Uniform Manifold Approximation and Projection (UMAP) analysis highlighting different passages in each replicate from (A) *PTEN*$^{-/-}$*;NF1*$^{-/-}$ and (B) *TP53*$^{-/-}$*;PDGFRA*$^{wt/\Delta 8\text{-}9}$ iGBMs.

		CASP1	CASP4	CASP5	CASP8	TRADD	TLR2	TLR4	RELB
P-S1	log2 fold	2.93	1.59	-18.49	1.47	1.19	1.89	-1.87	-0.26
	pvals_adj	6.34E-89	4.16E-136	1.00E+00	4.20E-36	4.12E-58	6.80E-01	6.14E-01	4.50E-01
P-T2.1	log2 fold	1.65	1.61	1.93	0.60	0.50	1.49	-1.27	-0.97
	pvals_adj	9.95E-12	3.07E-91	1.00E+00	8.79E-03	1.21E-05	9.66E-01	9.00E-01	5.03E-03
P-T2.2	log2 fold	0.21	0.67	0.63	-0.09	-0.17	-1.52	-2.30	-2.12
	pvals_adj	7.63E-01	4.99E-11	1.00E+00	1.00E+00	7.78E-01	1.00E+00	8.01E-01	4.76E-05
P-T2.3	log2 fold	1.46	1.50	-0.06	0.89	0.38	0.47	-1.56	-0.87
	pvals_adj	1.88E-10	1.64E-83	1.00E+00	1.90E-08	7.23E-04	1.00E+00	7.69E-01	6.42E-03
P-S2.1	log2 fold	2.03	1.56	-18.43	1.55	1.36	1.09	1.70	-0.21
	pvals_adj	1.03E-14	1.12E-57	1.00E+00	2.23E-18	4.35E-32	1.00E+00	2.07E-01	9.72E-01
P-S2.2	log2 fold	2.29	1.62	0.98	1.68	1.54	0.46	0.56	0.31
	pvals_adj	2.98E-19	7.23E-58	1.00E+00	2.47E-22	3.22E-43	1.00E+00	1.00E+00	4.62E-01
P-S2.3	log2 fold	1.52	1.35	-18.42	1.58	1.43	0.51	0.93	-0.09
	pvals_adj	1.12E-05	7.36E-29	1.00E+00	2.84E-15	1.21E-29	1.00E+00	1.00E+00	1.00E+00
T-S1	log2 fold	-3.73	-4.42	-1.66	-0.05	-0.20	-3.22	-1.32	0.23
	pvals_adj	3.46E-10	1.93E-100	1.00E+00	1.00E+00	1.79E-01	8.75E-01	4.77E-01	1.50E-01
T-T2.1	log2 fold	-5.92	-1.38	-18.42	-1.30	-2.48	0.20	-0.51	-1.01
	pvals_adj	1.81E-02	4.76E-07	1.00E+00	1.11E-02	3.62E-12	1.00E+00	1.00E+00	3.43E-02
T-T2.2	log2 fold	-3.04	-1.82	-18.43	-0.80	-2.56	-0.78	-0.08	-1.47
	pvals_adj	2.02E-02	4.60E-11	1.00E+00	7.38E-02	1.18E-14	1.00E+00	1.00E+00	2.78E-03
T-T2.3	log2 fold	-3.74	-0.93	0.37	-0.23	-0.79	-2.79	-0.77	-0.05
	pvals_adj	4.33E-03	2.58E-06	1.00E+00	6.57E-01	3.93E-05	1.00E+00	1.00E+00	9.49E-01
T-S2.1	log2 fold	-7.70	-0.59	1.88	-2.24	-1.61	0.27	0.26	-0.01
	pvals_adj	3.76E-19	1.78E-12	1.00E+00	2.11E-33	1.46E-65	1.00E+00	9.31E-01	1.00E+00
T-S2.2	log2 fold	-1.70	-0.12	-0.26	-0.31	-0.41	-0.01	0.27	0.47
	pvals_adj	6.54E-03	8.92E-01	1.00E+00	4.78E-01	8.02E-03	1.00E+00	1.00E+00	1.37E-02
T-S2.3	log2 fold	-4.00	-2.61	-2.37	-1.05	-0.02	-1.60	0.81	0.55
	pvals_adj	2.58E-16	6.62E-117	1.00E+00	5.26E-13	1.00E+00	9.57E-01	4.19E-01	3.38E-07

Table. S1
Fold-change in expression of the signature genes for mesenchymal subtype in each sample.

		DLL3	NKX2-2	SOX2	ERBB3	OLIG2
P-S1	log2 fold	0.25	-26.08	-3.11	-3.56	-26.70
	pvals_adj	3.77E-14	2.97E-09	2.79E-137	1.47E-48	1.96E-20
P-T2.1	log2 fold	-1.47	-26.04	-2.56	-0.29	-4.15
	pvals_adj	8.64E-55	5.75E-06	1.10E-74	3.90E-03	4.89E-11
P-T2.2	log2 fold	-1.85	-26.02	-2.40	0.35	-5.65
	pvals_adj	1.60E-51	1.06E-04	6.41E-51	1.65E-01	2.92E-09
P-T2.3	log2 fold	-1.70	-26.05	-3.44	-1.04	-5.33
	pvals_adj	2.61E-72	6.40E-07	1.13E-108	8.17E-15	5.99E-14
P-S2.1	log2 fold	-1.01	-26.02	-3.19	-1.85	-7.43
	pvals_adj	6.98E-21	5.23E-04	1.37E-55	7.56E-11	3.66E-08
P-S2.2	log2 fold	-0.77	-26.01	-3.32	-1.81	-26.63
	pvals_adj	3.47E-15	9.96E-04	1.16E-52	5.53E-10	1.23E-07
P-S2.3	log2 fold	-0.71	-26.00	-3.54	-1.61	-26.62
	pvals_adj	1.77E-09	4.32E-03	6.29E-44	8.65E-07	3.38E-06
T-S1	log2 fold	0.75	-5.92	0.58	-0.92	-2.60
	pvals_adj	3.25E-105	2.64E-18	1.97E-114	2.54E-17	2.97E-25
T-T2.1	log2 fold	-0.27	-1.14	0.45	-0.59	-0.16
	pvals_adj	4.26E-05	1.35E-01	1.81E-03	7.55E-03	1.00E+00
T-T2.2	log2 fold	0.39	-3.45	0.56	-0.35	-0.26
	pvals_adj	1.77E-01	1.87E-03	1.09E-07	6.78E-02	1.00E+00
T-T2.3	log2 fold	-0.45	2.45	1.13	1.73	2.12
	pvals_adj	5.37E-10	5.66E-37	6.63E-78	5.73E-73	7.21E-55
T-S2.1	log2 fold	0.35	-2.59	-1.13	-0.74	-1.49
	pvals_adj	6.50E-52	7.69E-20	2.59E-164	8.91E-17	6.70E-23
T-S2.2	log2 fold	0.18	-4.10	-0.67	-0.73	-0.66
	pvals_adj	1.02E-05	1.57E-06	7.13E-06	1.86E-04	3.75E-01
T-S2.3	log2 fold	-0.12	3.49	1.62	1.58	2.73
	pvals_adj	2.86E-04	2.79E-207	0.00E+00	1.15E-239	3.35E-267

Table. S2
Fold-change in expression of the signature genes for proneural subtype in each sample.

		FBXO3	GABRB2	SNCG	MBP
P-S1	log2 fold	0.53	-1.70	-0.08	-0.93
	pvals_adj	2.58E-05	1.89E-05	2.10E-01	1.69E-01
P-T2.1	log2 fold	0.09	-4.73	-2.99	1.34
	pvals_adj	1.00E+00	1.51E-06	0.00E+00	1.16E-04
P-T2.2	log2 fold	-0.33	-5.78	-3.16	0.55
	pvals_adj	3.41E-01	2.66E-05	2.14E-245	4.29E-01
P-T2.3	log2 fold	-0.02	-6.46	-2.99	0.81
	pvals_adj	1.00E+00	5.62E-08	0.00E+00	1.24E-01
P-S2.1	log2 fold	1.13	-25.76	0.57	1.25
	pvals_adj	5.36E-13	1.13E-04	8.86E-53	7.83E-03
P-S2.2	log2 fold	1.14	-25.75	0.74	0.69
	pvals_adj	1.71E-12	2.47E-04	4.00E-78	4.52E-01
P-S2.3	log2 fold	0.93	-25.74	0.53	0.82
	pvals_adj	1.12E-05	1.43E-03	6.54E-33	2.91E-01
T-S1	log2 fold	-0.15	0.18	-0.73	-3.38
	pvals_adj	3.92E-01	1.78E-01	7.59E-151	5.70E-07
T-T2.1	log2 fold	-0.26	0.19	-0.86	-0.92
	pvals_adj	6.37E-01	1.00E+00	9.23E-42	7.09E-01
T-T2.2	log2 fold	-0.48	0.06	-1.10	-0.78
	pvals_adj	1.41E-01	1.00E+00	1.37E-66	5.98E-01
T-T2.3	log2 fold	0.15	0.71	-1.97	0.90
	pvals_adj	6.04E-01	4.54E-02	1.88E-192	2.67E-01
T-S2.1	log2 fold	-0.53	1.74	1.36	-1.45
	pvals_adj	8.03E-08	2.77E-52	0.00E+00	1.06E-04
T-S2.2	log2 fold	0.04	-1.26	0.28	0.47
	pvals_adj	1.00E+00	4.02E-03	2.86E-42	1.08E-01
T-S2.3	log2 fold	-0.26	-0.22	-0.21	0.59
	pvals_adj	1.71E-02	4.18E-01	8.83E-26	2.00E-02

Table. S3
Fold-change in expression of the signature genes for neural subtype in each sample.

		FGFR3	PDGFA	EGFR	AKT2	NES
P-S1	log2 fold	-3.35	-3.75	1.16	0.01	-2.08
	pvals_adj	1.44E-02	1.79E-04	2.05E-06	1.00E+00	0.00E+00
P-T2.1	log2 fold	2.89	-2.93	-0.05	-0.22	-0.54
	pvals_adj	4.00E-26	9.58E-03	1.00E+00	4.52E-03	4.73E-58
P-T2.2	log2 fold	0.78	-1.85	-0.18	-0.57	-0.30
	pvals_adj	3.90E-01	1.07E-01	9.87E-01	1.06E-11	3.38E-18
P-T2.3	log2 fold	2.63	-1.77	-0.41	-0.22	-0.85
	pvals_adj	2.75E-20	2.56E-02	5.56E-01	7.72E-04	9.40E-123
P-S2.1	log2 fold	0.74	-3.37	-0.78	-0.21	-0.16
	pvals_adj	3.39E-01	4.42E-02	4.46E-01	2.83E-02	2.04E-04
P-S2.2	log2 fold	0.90	-3.72	-0.75	-0.20	0.10
	pvals_adj	2.89E-01	4.79E-02	5.19E-01	4.79E-02	2.29E-01
P-S2.3	log2 fold	0.69	-3.34	-1.64	-0.33	-0.06
	pvals_adj	6.28E-01	9.56E-02	2.15E-01	4.10E-03	4.80E-01
T-S1	log2 fold	-0.99	-1.87	1.53	-0.57	0.14
	pvals_adj	1.22E-01	4.37E-05	5.70E-19	5.48E-42	3.07E-18
T-T2.1	log2 fold	-1.12	-0.77	-1.19	-0.84	0.20
	pvals_adj	7.68E-01	7.21E-01	3.05E-01	5.70E-16	1.02E-04
T-T2.2	log2 fold	-0.07	-1.91	-1.22	-0.75	0.24
	pvals_adj	1.00E+00	1.22E-01	2.07E-01	5.19E-16	5.71E-09
T-T2.3	log2 fold	-0.89	2.45	-1.09	-0.15	0.00
	pvals_adj	6.80E-01	2.06E-21	1.56E-01	8.68E-02	7.26E-01
T-S2.1	log2 fold	-3.29	-1.33	0.06	0.44	0.44
	pvals_adj	1.33E-06	2.46E-04	9.23E-01	6.35E-56	6.09E-236
T-S2.2	log2 fold	-2.37	-1.99	-1.77	-0.15	-0.25
	pvals_adj	7.80E-02	1.77E-02	8.15E-03	1.12E-02	5.85E-12
T-S2.3	log2 fold	-0.96	2.43	-1.36	0.41	0.24
	pvals_adj	7.09E-02	3.61E-47	2.31E-06	6.90E-48	4.18E-55

Table. S4
Fold-change in expression of the signature genes for classical subtype in each sample.